

INTERACTION OF CONCENTRATED NaCl SOLUTIONS WITH HYDROPHILIC AND HYDROPHOBIC FUMED SILICAS

Volodymyr M. Gun'ko^{1,*}, Mykola V. Borysenko¹, Alina P. Holovan¹, Tetyana V. Krupskaya^{1,2}, Qiliang Wei², Jinju Zheng², Weiyou Yang², Volodymyr V. Turov^{1,2}

¹Chuiko Institute of Surface Chemistry, 17 Oleh Mudrak Str., Kyiv 03164, Ukraine,
e-mail: vlad_gunko@ukr.net

²Institute of Micro/Nano Materials and Devices, Ningbo University of Technology,
Ningbo City 315211, P.R. China

In porous or disperse media, the temperature and interfacial behaviors of water and solutions could be strongly affected by confined space effects (CSE). The surface nature of solids could influence the interfacial phenomena including both CSE and cryoscopic effects caused by the colligative properties of solutions. Strong changes in the characteristics of adsorption liquid layers, especially in narrow pores, are also caused by decreasing solvent activity. Therefore, it is of interest to compare the behaviors of water and NaCl solutions under CSE caused by hydrophilic and hydrophobic sorbents. Here, hydrophobic (AM–1) and hydrophilic (A–300) fumed silicas are used as representatives of disperse sorbents with different surface structure and characterized by textural porosity. This porosity is caused by voids between nonporous nanoparticles (NPNP) forming aggregates, agglomerates of aggregates, and visible particles (supra-NP structures) in the powders of low bulk density. Initial materials and related treated systems with bound water and NaCl/water were studied using nitrogen adsorption, microscopy, X–ray diffraction, infrared spectroscopy, thermogravimetry, rheometry, nuclear magnetic resonance spectroscopy, and quantum chemistry. Water bound to fumed silicas with or without NaCl could be assigned to several types: weakly (WBW, frozen at $260\text{ K} < T < 273\text{ K}$) and strongly (SBW, frozen at $T < 260\text{ K}$) bound waters; weakly (WAW, chemical shift of $\delta_H = 0.5 - 2\text{ ppm}$) and strongly (SAW, $\delta_H = 4 - 6\text{ ppm}$) associated waters. WAW is not observed for A–300 systems. Additionally, in the systems with water/NaCl, there is frozen (immobile) water characterized by melting delay ($T > T_m$) at $273\text{ K} < T < 287\text{ K}$ (metastable water, MSW). The MSW appearance may be explained by release (with certain kinetic delay) of water trapped in NaCl crystallites dissolved at $T > T_m = 273.15\text{ K}$ upon increasing amounts of liquid water with increasing temperature. The difference in the CSE in voids in hydrophobic and hydrophilic supra-NP structures onto bound water could be explained by the surface $(-O)_2Si(CH_3)_2$ functionalities enhancing the clusterization of water bound to AM–1. As a whole, the difference in the surface nature of AM–1 and A–300 affects: (i) the NaCl crystallite size distributions; (ii) melting/crystallization temperatures of NaCl; (iii) viscosity and torque vs. shear rate (strain); (iv) temperature and interfacial behaviors of water alone and NaCl solutions at $215 - 287\text{ K}$; and (v) effects of dispersion media influencing bound water. Obtained results are of interest not only from a theoretical point of view but also from a practical one since both silicas are used as components of composites containing water and NaCl (or other salts) in various practical applications in medicine, agriculture, etc.

Keywords: hydrophobic fumed silica, hydrophilic fumed silica, concentrated NaCl solution, interfacial water, confined space effects, cryoscopic effects, interfacial solution behavior, temperature behavior.

1. INTRODUCTION

Sodium chloride is an important component of seawater and biological fluids, and it is involved in many geo- and bio-processes. In aqueous solutions, dissolved Cl^- and Na^+ ions have solvation shells with several layers with water molecules [1 – 3]. The water molecules in a liquid phase form a system of clusters and domains [2] binding in the hydrogen bond network (HBN); however, interstitial molecules are also present without strong hydrogen bonds [1 – 7]. The dissolved ions can affect the HBN in bulk and pore-confined water. The diffraction of slow neutrons in NaCl and KCl solutions with various salt concentrations shows that water molecules in the hydration shells of K^+ ions are more orientationally disordered than those around Na^+ ions, and tend to orient the dipole moments tangential to the hydration sphere. The Cl^- ions form the hydrogen bonds ($\text{Cl}^- \cdots \text{H}-\text{OH}$) with water molecules and can be easily integrated into the water HBN [3]. The rotational spectra of NaCl solutions with different concentrations [4] show that water clusters have a cyclic shape, in which Na^+ and Cl^- ions interact strongly with the O and H atoms of water, respectively, and the Na–Cl distance increases with decreasing NaCl concentration. The structure of the hydration shells of ions of alkali metal chlorides was analyzed using computer modeling [6–8]. Special attention was paid to study the question of how strongly alkali metal ions distort the HBN structure of liquid water. For Na, K, and Cs, the ability of ions of different sizes to exert both ordering/disordering effects on the HBN has been shown [2]. The quasi-elastic neutron scattering [9] using heavy water solutions shows a different behavior in the ordering of the hydration shell of ions for kosmotropics compared to solutions of chaotropic ions. This effect increases with salt concentration for the former and decreases for the latter [2]. In both cases, the trends are proportional to the concentration dependence of the solution viscosity. These results show that kosmotropics and chaotropics can influence the viscosity due to changes in the water HBN in opposite ways, strengthening it in the first case and destabilizing it in the second one. The hydration entropy and effects on the viscosity of the Na^+ and Cl^- ions are smaller than that of other ions [2]. The ordering/disordering effects of the Na^+ and Cl^- ions on the water HBN are minimal according to the Hofmeister series [2] that is of importance for the bio-processes. The mentioned effects of the Na^+ and Cl^- ions explain a relatively weak freezing point depression (FPD) of the aqueous solutions (with the colligative properties giving cryoscopic effects, CE), and the eutectic point is at 252.05 K and 23.3 wt. % NaCl (Fig. 1a) [2, 10 – 14]. Note that the CE for water/dimethyl sulfoxide (DMSO is a weakly kosmotropic solvent) are much stronger, since the eutectic points are at 200–210 K (Fig. 1b), than that for water/NaCl (Fig. 1a).

Various external factors, *e.g.*, excess pressure [15], magnetic fields [16, 17], confined space effects (CSE) [18 – 25], or the presence of co-solvents and solutes [26 – 28] can affect the structure of the hydration shells of ions, as well as the whole HBN structure. For example, the X-ray diffraction (XRD) data [15] show that the coordination number of the salt ions increases from 6 (at 0.1 MPa) to approximately 16 at 1.7 GPa. An increase in the pressure is accompanied by a significant expansion of the solvation shells of the salt ions. This process can significantly influence the formation of hydrocarbon hydrates in the bottom seawater layers [29 – 34]. For example, since the formation of methane hydrates often occurs near or inside bottom sediments, the dynamics of the hydrate formation and decomposition could change due to the presence of the Na^+ and Cl^- ions. However, the methane hydrates form much more easily in bulk water than in pore-confined water [35], since CSE can significantly affect the structure of water and hydration shells of the salt ions. These effects could also depend on hydrophilicity/hydrophobicity of porous media. Therefore, it is of interest to compare the temperature and interfacial behaviors of NaCl solutions in water bound to hydrophobic and hydrophilic adsorbents, *e.g.*, fumed silicas. These silicas are composed of nonporous nanoparticles (NPNP) forming aggregates ($< 1 \mu\text{m}$ in size), agglomerates of aggregates (1 – 50 μm), and visible loose particles in the powders characterized by very low bulk density

($\sim 0.05 \text{ g/cm}^3$). Three last kinds of mentioned structures could be assigned to supra-NP ones, which can be easily decomposed due to any external actions (wetting, drying, stirring, *etc.*) affecting the properties and characteristics of whole systems.

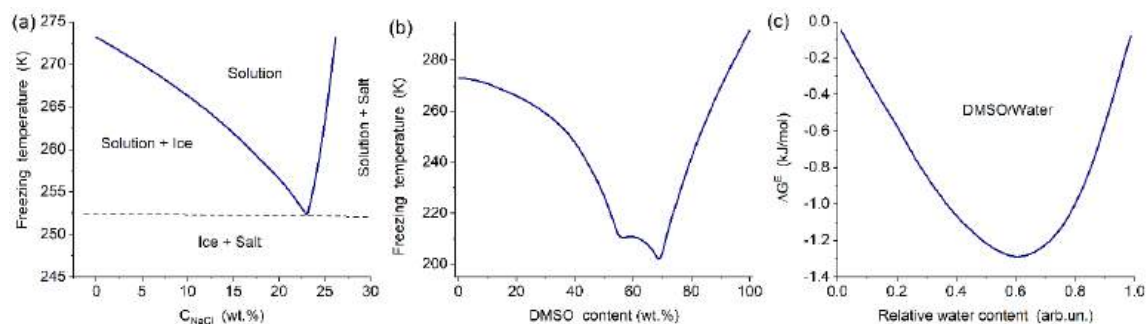


Fig. 1. State diagram of (a) NaCl-water [10 – 14]; (b) DMSO-water; and (c) changes in the Gibbs free energy for DMSO/water mixtures

Thus, a study of the temperature and interfacial behaviors of aqueous solutions of NaCl (characterized by the colligative properties) under CSE/CE in different dispersion media is of interest from theoretical and practical points of view [1 – 9, 18–25, 36 – 40]. The interfacial phenomena in a wide temperature range (including $T < T_f$, freezing temperature) are complex since they depend on a lot of factors. Therefore, the aim of this work was to study the state of water alone and in concentrated NaCl solutions bound to nanoparticles of hydrophobic (AM–1) and hydrophilic (A–300) fumed silicas in different dispersion media in wide ranges of temperature and water/NaCl concentrations using several methods applied to both wetted silica and NaCl/silica samples (low-temperature ^1H nuclear magnetic resonance (NMR) spectroscopy, thermogravimetry (TG), rheometry, XRD, infrared (IR) spectroscopy) and dried degassed native silicas (nitrogen adsorption, transition (TEM) and scanning (SEM) electron microscopy).

2. MATERIALS AND METHODS

2.1. Materials

Fumed nanosilicas, dimethyldichlorosilane modified A–200 (AM–1, specific surface area $S_{\text{BET}} = 178 \text{ m}^2/\text{g}$, bulk density $\rho_b \approx 0.05 \text{ g/cm}^3$) and hydrophilic A–300 ($S_{\text{BET}} = 294 \text{ m}^2/\text{g}$, $\rho_b \approx 0.05 \text{ g/cm}^3$) (Pilot plant of Chuiko Institute of Surface Chemistry, Kalush, Ukraine) were used to study the interactions with NaCl/water of different amounts. One gram of dry AM–1 powder was stirred in a porcelain mortar to form a compacted material with a bulk density $\rho_b \approx 0.2 \text{ g/cm}^3$. The NaCl solutions were prepared in two ways. A mixture of salt and water was equilibrated at room temperature for one hour with periodic stirring, and then a supernatant fraction (with *ca.* 26.4 wt. % NaCl) was used to add to compacted AM–1. After stirring the mixture for several minutes, the solution effectively infills interparticle voids of fumed silica to form a homogeneous system [41]. Similar systems were studied using low-temperature ^1H NMR spectroscopy [41] and cryoporometry [41 – 44]. Two samples of AM–1 treated with added NaCl solution contain 120 and 240 mg/g of water and 43.2 and 86.4 mg/g of NaCl, respectively. Additionally, a 1:1 mixture of water and NaCl was stirred and then added to AM–1 ($2\text{NaCl}/2\text{H}_2\text{O}/1\text{AM–1}$) and treated again during several minutes to form uniform blend at contents $C_{\text{NaCl}} = h$ (hydration degree) = 2 g per gram of dry silica). Similar blends were prepared with A–300/NaCl/water that gives two samples at $h = 0.15$ and 1 g/g and $C_{\text{NaCl}} = 0.15$ and 1.0 g/g (with respect to dry silica), respectively. It should be noted that the initial amounts of water bound to AM–1/NaCl and A–300/NaCl could diminish due to evaporation during measurements using different methods.

2.2. Textural characteristics of nanosilicas

To analyze the textural characteristics of initial non-compacted nanosilicas (composed of nonporous nanoparticles, NPNP) degassed at 353 K or 373 K for several hours, low-temperature (77.4 K) nitrogen adsorption–desorption isotherms (Fig. 2a) were recorded using a Micromeritics ASAP 2420 adsorption analyzer. The specific surface area (Table 1, S_{BET}) values were calculated according to the standard BET method [45]. The total pore volume (V_p) values were estimated from the nitrogen adsorption at $p/p_0 \approx 0.98 - 0.99$, where p and p_0 denote the equilibrium and saturation pressure of nitrogen at 77.4 K, respectively [46].

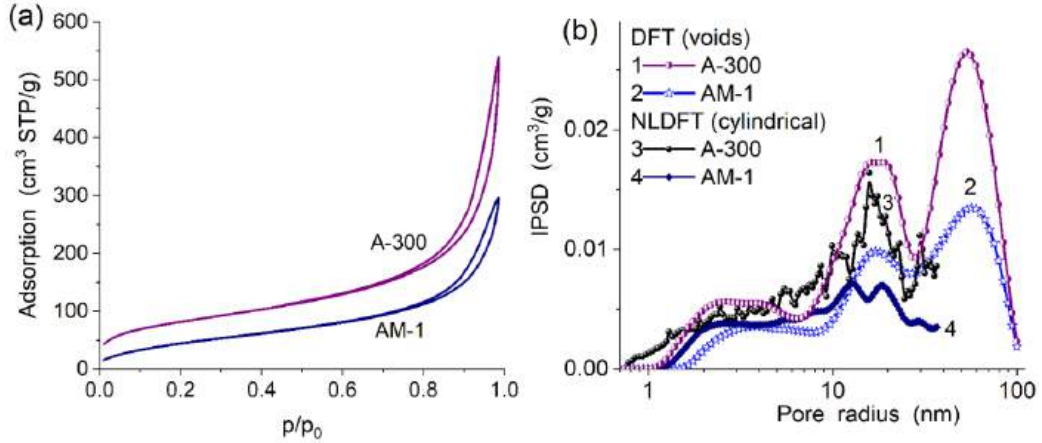


Fig. 2. (a) Nitrogen adsorption-desorption isotherms (at 77.35 K) for nanosilicas A-300 and AM-1; and (b) incremental pore size distributions (IPSD) for these silicas calculated using the isotherms treated with NLDFT and DFT methods

Table 1. Textural characteristics of initial individual silicas with the DFT method

Sample	S_{BET} (m^2/g)	S_{nano} (m^2/g)	S_{meso} (m^2/g)	S_{macro} (m^2/g)	V_p (cm^3/g)	V_{nano} (cm^3/g)	V_{meso} (cm^3/g)	V_{macro} (cm^3/g)	$\langle R_V \rangle$ (nm)	$\langle R_S \rangle$ (nm)
AM-1	178	84	84	10	0.466	0.025	0.272	0.169	25.1	6.5
A-300	294	102	171	21	0.524	0.016	0.259	0.248	30.3	6.7

Note. The values of V_{nano} and S_{nano} were calculated by integration of the $f_V(R)$ and $f_S(R)$ functions, respectively, at $0.35 \text{ nm} < R < 1 \text{ nm}$, V_{meso} and S_{meso} at $1 \text{ nm} < R < 25 \text{ nm}$, and V_{macro} and S_{macro} at $25 \text{ nm} < R < 100 \text{ nm}$.

A pore model corresponding to voids between spherical NPNP packed in random aggregates was used in density functional theory (DFT) method [47] to calculate the pore size distributions (PSD) with respect to the pore volume ($f_V(R)$) (Fig. 2b) and specific surface area ($f_S(R)$). The $f_V(R)$ and $f_S(R)$ DFT functions were used to calculate contributions of nanopores (V_{nano} and S_{nano} at $0.35 \text{ nm} < R < 1 \text{ nm}$), mesopores (V_{meso} and S_{meso} at $1 \text{ nm} < R < 25 \text{ nm}$), and macropores (V_{macro} and S_{macro} at $25 \text{ nm} < R < 100 \text{ nm}$). The values of $\langle R_V \rangle$ and $\langle R_S \rangle$ as the average pore radii were calculated as a ratio of the first moment of $f_V(R)$ or $f_S(R)$ to the zero moment (integration was done over the $0.35 (R_{\text{min}}) - 100 (R_{\text{max}})$ nm range) ($x = V$ or S in Eq. (1))

$$\langle R_x \rangle = \frac{\int_{R_{\text{min}}}^{R_{\text{max}}} f_x(R) R dR}{\int_{R_{\text{min}}}^{R_{\text{max}}} f_x(R) dR} \quad (1)$$

Additionally, nonlocal DFT (NLDFT) method (Quantachrome software) was used with a model of cylindrical pores in silica to compute the PSD (Fig. 2b).

2.3. Scanning (SEM) and transmission (TEM) electron microscopy

TEM (TECNAI G2 F30 microscope (FEI–Philips), operating voltage 300 kV) was used to analyze the particulate morphology of samples. The powder samples were added to acetone (chromatographic grade) and sonicated. A suspension drop was then deposited onto a copper grid covered by a thin carbon film. After acetone evaporation, the dry sample remaining on the film was studied. SEM (FE–SEM, Hitachi S–4700, Tokyo, Japan, operating voltage of 15 kV, and magnification of $\times 5000$ – 100000 or QuantaTM 3D FEG, FEI, USA, voltage of 15 kV) was used to analyze the morphological features of the initial powder nanosilicas. The images show aggregates of nanoparticles, agglomerates of aggregates, and various voids between nanoparticles.

2.4. X-ray diffraction (XRD)

X–ray diffraction patterns were recorded over $2\theta = 5 - 70^\circ$ range using a DRON–3M (Burevestnik, St. Petersburg) diffractometer with Cu $K\alpha$ ($\lambda = 0.15418$ nm) radiation and a Ni filter. According to XRD patterns, hydrophobic nanosilica AM–1 treated with water and NaCl/water is amorphous as well as hydrophilic nanosilica A–300. NaCl (both dissolved and non-dissolved) forms crystallites upon water evaporation.

The XRD data could be used for simple estimation of average sizes of crystallites using Scherrer or Debye–Scherrer equations [48, 49]. Additionally, the XRD data could be used to estimate the crystallite size distribution (CSD) functions using full profile analysis of selected lines or total XRD patterns [50 – 52]. To calculate the broadened line (pure) profile related to the crystallite size/faulting effects of materials studied, as well a size distribution function, one could use two integral equations [50 – 52]:

$$I_{ex.obs.}(\varepsilon) = C \int h_{i.p.}(\varepsilon - t) i_{ex.pure}(t) dt, \quad (2)$$

$$i(s) = \int_{D_{min}}^{D_{max}} D \frac{\sin^2(\pi s D)}{(\pi s D)^2} g(D) dD, \quad (3)$$

where $I_{ex.obs.}(\varepsilon)$ is the experimentally observed X-ray diffraction profile, C is a constant, $h_{i.p.}$ is the instrumental profile, $i(s)$ is the pure crystallite size/faulting profile, D is the crystallite size, $g(D)$ is the CSD function, 2θ is the scattering angle, $2\theta_{hkl}$ is the scattering angle corresponding to a peak

$$s = s_{2\theta} - r_{hkl} = 2(\sin \theta) / \lambda - 2(\sin \theta_{hkl}) / \lambda. \quad (4)$$

The variable ε in Eq. (2) corresponds to the angular deviation of a point from the true Bragg angle $2\theta_0$; and ε and the auxiliary variable t have the dimension of 2θ . The CSD function $g(D)$ could be computed by solving integral Eq. (2) and then Eq. (3) (note that Eq. (3) corresponds to spherical crystallites) with a regularization procedure [52, 53]. This approach could be applied to a selected line or to the full profile of total XRD patterns analyzed after background subtraction and normalization.

2.5. Infrared spectroscopy

Infrared spectra of the studied samples were recorded using a Fourier transform infrared (FTIR) IRTracer–100 (Shimadzu) spectrophotometer with a diffuse reflectance (DR) attachment DRS–8000A. The infrared spectra were also recorded in the range of $4000 - 300$ cm^{-1} using a Specord M80 (Carl Zeiss) spectrometer. To record the IR spectra, samples with A–300 or AM–1 alone or with KBr (1 : 300) were pressed into thin pellets (~ 20 mg).

2.6. Thermogravimetry

Thermograms (thermogravimetry, TG at the average weight errors ± 0.1 mg, differential TG, DTG, and differential thermal analysis, DTA data) were recorded using a Derivatograph Q-1500 D apparatus (Paulik, Paulik & Erdey, MOM, Budapest, Hungary) upon heating of samples (~ 0.2 g) in air at a heating rate of 10 °C/min from 20 to 1000 °C. The TG curves show that the amounts of water in samples under measurements are smaller than the initial ones due to water evaporation upon sample preparation.

2.7. Rheometry

Rheometric measurements (in air at 20 °C) were carried out using an MCR 92 (Anton Paar, Austria) rheometer in a rotational mode (with a rotated disk) with RheoCompass™ software. The starting value of shear strain was 0.05 % increased to 60 % (shear rate $\dot{\gamma} = 0.05 - 100.0$ s $^{-1}$) and then reduced to 0.05 %. Before the rheometric measurements, all samples (with 0.5 g of air-dry silicas) were stirred without and then with added water up to 7 min.

The colloidal or gel-like systems are energetically nonuniform with respect to conditions of the motion of particles or molecules between different coagulation clusters (cages) because of their structural hierarchy. Therefore, the activation energy (E) of interparticle bond breakage linked to the shear viscosity corresponding to this motion (modelled as jumps of particles or molecules between different cages, *i.e.*, clusters) can be determined in the form of a distribution function $f(E)$ [54]

$$\eta(T, \dot{\gamma}) = \eta_{\infty} + (\eta_0 - \eta_{\infty}) \int_{E_{\min}}^{E_{\max}} \frac{1}{z} \int_0^z \frac{dx}{\sqrt{1+x^2}} f(E) dE, \quad (5)$$

with the kernel $\frac{\sinh^{-1}(\beta' \dot{\gamma})}{\beta' \dot{\gamma}}$, where E_{\min} and E_{\max} are the limits of integration and

$$z = \beta' \dot{\gamma} = c \dot{\gamma} \frac{a^2}{D_0} \frac{k_B T}{E} \exp\left(\frac{E}{k_B T}\right) = A' \dot{\gamma} \frac{k_B T}{E} \exp\left(\frac{E}{k_B T}\right). \quad (6)$$

Solution of Eq. (5) is well known ill-posed problem due to the impact of noise on measured data, which does not allow one to utilize exact inversion formulas or iterative algorithms. Therefore, Eq. (5) can be solved using a regularization procedure based on the CONTIN algorithm [53, 54] under condition of nonnegativity $f(E) \geq 0$ at any E and fixed or unfixed regularization parameter determined by statistical analysis of the experimental data.

2.8. NMR spectroscopy and cryoporometry

Low-temperature ^1H NMR spectra of static samples were recorded using a high-resolution NMR spectrometer (Varian 400 “Mercury”) with an operating frequency of 400 MHz. Eight 60° probe pulses were used with a duration of 1 μs and a bandwidth of 20 kHz. The temperature was regulated using a Bruker VT-1000 thermal attachment with an accuracy of ± 1 degree. Signal intensities were determined by measuring peak areas using a signal decomposition procedure assuming a Gaussian waveform and optimizing the zero line and phase with an accuracy of at least 5 % for well-resolved signals and ± 10 % for overlapping signals. To prevent overcooling of water in the objects under study, measurements of the concentration of unfrozen water were carried out by heating of samples pre-cooled to $210 - 215$ K. Temperature dependences of the intensity of ^1H NMR signals were carried out in an automated cycle, when the sample was kept at a constant temperature for 5 min, and the measurement time was 1 min.

The process of freezing (thawing) of water bound to solids occurs with changes in the Gibbs free energy caused by the influence of a solid surface, confined space effects, solutes, colligative properties of solutions (cryoscopic effects), and co-solvents. Frozen water does not contribute the recorded ^1H NMR signals due to a narrow bandwidth of 20 kHz and a large difference in the transverse relaxation time of mobile (liquid water and solutions) and immobile (frozen water, solids) phases [41]. Water (or other liquids) can be frozen in narrower pores (or voids between nanoparticles) at lower temperatures as described by the Gibbs–Thomson relation for the freezing point depression for liquids confined in cylindrical pores at radius R [41–44]. This relation is the base of cryoporometry giving information of the size distributions of pores (voids) infilled by unfrozen water.

The area under $\Delta G(C_{uw})$ curve determines the modulus of the total changes in the Gibbs free energy ΔG vs. the amount of unfrozen water (C_{uw}) that are caused by interactions of water with silica and NaCl crystallite surfaces [41]

$$\gamma_S = -A \int_0^{C_{uw}^{\max}} \Delta G(C_{uw}) dC_{uw}, \quad (7)$$

where C_{uw}^{\max} is the total amount of water unfrozen at $T = 273$ K, and A (> 0) is a constant dependent on the type of units used in this equation.

Water can be frozen in narrower pores (or voids between nanoparticles) at lower temperatures as described by the Gibbs–Thomson relation for the freezing point depression for liquids confined in cylindrical pores at radius R [41 – 44]

$$\Delta T_m = T_{m,\infty} - T_m(R) = -\frac{2\sigma_{sl}T_{m,\infty}}{\Delta H_f \rho R} = \frac{k_{GT}}{R}, \quad (8)$$

where $T_m(R)$ is the melting temperature of ice in cylindrical pores of radius R , $T_{m,\infty}$ the bulk melting temperature, ΔH_f the bulk enthalpy of fusion, ρ the density of the solid, σ_{sl} the energy of solid–liquid interaction, and k_{GT} is the Gibbs–Thomson constant (here $k_{GT} = 67$ K nm for water). Eq. (8) was used to determine the void size distributions (VSD) (differential $f_V(R) = dV_{uw}(R)/dR$) filled by bound water unfrozen at $T < 273$ K [55]. Integration of the $f_V(R)$ and $f_S(R)$ functions at $0.2 \text{ nm} < R < 1 \text{ nm}$, $1 \text{ nm} < R < 25 \text{ nm}$, and $25 \text{ nm} < R < 100 \text{ nm}$ gives the volume and specific surface area of nano-, meso- and macrovoids (pores), respectively, being in contact with unfrozen liquids. The specific surface area (S_{uw}) of adsorbents in contact with bound water (assuming for simplicity that the density of unfrozen bound water $\rho_{uw} = 1 \text{ g/cm}^3$) can be determined from the amount of this water C_{uw}^{\max} (estimating pore volume as $V_{uw} = C_{uw}^{\max} / \rho_{uw}$) at $T = 273.15$ K and pore size distribution $f(R)$ with a model of cylindrical pores [55]

$$S_{uw} = \frac{V_{uw}}{2R_{av}} = \frac{2C_{uw}^{\max}}{\rho_{uw}} \left(\int_{R_{\min}}^{R_{\max}} f(R) dR \right) / \left(\int_{R_{\min}}^{R_{\max}} f(R) R dR \right), \quad (9)$$

where R_{\min} and R_{\max} are the minimal and maximal radii of pores filled by unfrozen water, respectively. In the case of calculations of the structural characteristics of nanovoids ($R < 1 \text{ nm}$), mesovoids ($1 \text{ nm} < R < 25 \text{ nm}$) and macrovoids ($R > 25 \text{ nm}$), the R_{\min} and R_{\max} values are the boundary R values for the corresponding void types (including $R_{\min} = 0.2 \text{ nm}$ for nanovoids). The $C_{uw}^{\max} / \rho_{uw}$ value should be replaced by the corresponding values of the volumes of nanovoids,

mesovoids, and macrovoids [41]. The average melting temperature $\langle T_m \rangle$ was calculated using formula [55]

$$\langle T_m \rangle = \left(\int_{T_{\min}}^{T_0} TC_{uw}(T) dT \right) / \left(\int_{T_{\min}}^{T_0} C_{uw}(T) dT \right), \quad (10)$$

where $T_0 = 273.15$ K, and T_{\min} is the temperature corresponding to $C_{uw} = 0$.

Solid-state ^1H magic-angle spinning (MAS) NMR spectra were recorded using an Agilent DD2 600 MHz NMR spectrometer (Agilent, USA, magnetic field 14.157 T). A powder sample in a 4.0 mm pencil-type zirconia rotor was rotated at 8 kHz with a recycle delay of 5 s. Adamantane was used as a reference to estimate the chemical shift of proton resonance (δ_{H}). Solid-state ^{29}Si cross-polarization (CP)/MAS NMR spectra were recorded using the same equipment at a resonance frequency of 199.13 MHz for ^{29}Si using CP/MAS and high-power ^1H decoupling (spinning at 8 kHz, 4 μs 90° pulses, 2 ms CP pulse, and a recycle delay of 3 s), and tetramethylsilane (TMS) as a reference for the ^{29}Si chemical shift ($\delta(^{29}\text{Si})$).

The $\delta_{\text{H}}(T)$ function depends on the number of possible configurations of the water molecules in the hydrogen bonds network strongly affected by hydrophilic and hydrophobic or mosaic functionalized surroundings and dispersion media [56, 57]. This number is inversely proportional to the average number of the hydrogen bonds $\langle n_{\text{HB}} \rangle$, according to the hydrogen bond entropy definition as $S \approx -k_B \ln n_{\text{HB}}$ [56]. The temperature derivative of the measured fractional chemical shift [56]

$$-\left(\frac{\partial \ln \delta(T)}{\partial T} \right)_p = -\left(\frac{\partial \ln \langle n_{\text{HB}} \rangle}{\partial T} \right)_p \approx \left(\frac{\partial S}{\partial T} \right)_p \quad (11)$$

should be proportional to the constant pressure specific heat $C_P(T)$ ($C_P = T(\partial S/\partial T)_P$). This aspect was analyzed in detail elsewhere [56].

2.9. Quantum chemistry

Quantum chemical (QC) calculations using density functional theory (DFT) method were carried out using a hybrid functional $\omega\text{B97X-D}$ with the cc-pVDZ basis set with the Gaussian 16 C.02 [58], GAMESS 2024 R2 [59, 60], AMS 2024.1 [61] or semiempirical PM7 (MOPAC 2022.1.1) [62], DFTB+ (ver. 24.1) [63] (with some additional parameters [64]) methods with several program suits. The ^1H NMR spectra were calculated using the GIAO method [58–61]. The solvation effects were considered using SMD method [65]. Visualization of the computed models was carried out using several programs [66–69]. To compute the Gibbs free energy of solvation (subscript s), $\Delta G_s = G_l - G_g$, where G_l and G_g are the Gibbs free energies of a molecule free or bound to silica cluster in the liquid (subscript l) and gas (g) media, respectively. The calculations were performed taking into account zero-point and thermal corrections to the Gibbs free energy in the gas phase and for solvated molecules and silica clusters using the geometry optimized using $\omega\text{B97X-D/cc-pVDZ}$. Note that functional $\omega\text{B97X-D}$ introduces empirical damped atom-pairwise dispersion terms into the functional containing range-separated Hartree-Fock exchange for better description of van-der-Waals interactions. Therefore, this functional was selected to obtain more adequate results for the gas and liquid (SMD) phases with both hydrophilic and hydrophobic solvents. The distribution functions of the δ_{H} values were calculated using a simple equation [57]

$$f(\delta_H) = (2\pi\sigma^2)^{-0.5} \sum_j \frac{\exp[-(\delta_j - \delta_H)^2]}{2\sigma^2}, \quad (12)$$

where j is a number of H atom, σ^2 is the distribution dispersion, and δ_j is the calculated value of the j -th H atom. Large structures (up to 18000 atoms) were calculated using the PM7 method. To calculate the $f(\delta_H)$ functions using the PM7 results, a calibration function was used to describe the dependence between atomic charges q_H (PM7) and the δ_H values estimated

$$\delta_H = -27.38435372 + 83.67491184 \times q_H. \quad (13)$$

Eq. (13) was used to calculate the ^1H NMR spectra of water clusters alone and bound to silicas. To calculate the equation constants in Eq. (13) in linear approximation, the δ_H values were determined for several water clusters calculated using the GIAO/ ω B97X-D/cc-pVDZ method as the difference between nuclear magnetic shielding of tetramethylsilane (TMS) as standard (σ_{TMS}) and tested (σ) systems using isotropic values (magnetic shielding tensor spurs) $\sigma = (\sigma_{11} + \sigma_{22} + \sigma_{33})/3$. The same clusters were also calculated using the PM7 method to obtain the q_H values. Note that similar simple δ vs. q correlations are absent for non-hydrogen atoms due to complex factors affecting the magnetic shielding tensors of multi-electron atoms. Additionally, the equation (Eq. (13)) constants for H atoms in different compounds (e.g., various organics and inorganics) are different for different types of compounds and also depend on the types of ab initio or DFT and semiempirical (e.g., PM3, PM6, and PM7) methods used.

3. RESULTS AND DISCUSSION

3.1. Characterization of nanosilicas

Studied silicas represent loose powders (bulk density $\sim 0.05 \text{ g/cm}^3$) with nanoparticles forming aggregates and agglomerates of aggregates (Figs. 3 and 4) responsible for the textural porosity with various voids (see Fig. 2b) between the particles. The particulate morphology of AM-1 and A-300 is similar (Figs. 3 and 4), but AM-1 is composed of slightly larger nanoparticles with broader particle size distribution than those of A-300 (Fig. 5). Both AM-1 and A-300 silicas are composed of amorphous nanoparticles (Fig. 6a), which include nuclei (Fig. 6b) formed in the flame at high temperatures and densely packed in NPNP. The pore (void) size distributions (PSD) are broad for both silicas (Fig. 2b) with predominant contributions of mesopores ($1 \text{ nm} < R < 25 \text{ nm}$ in radius) and macropores ($R > 25 \text{ nm}$). After compaction or hydro-compaction of nanosilicas they are remained predominantly meso/macroporous with the pore volume of $V_p = 1.5 - 2.5 \text{ cm}^3/\text{g}$ [41, 70 - 72]. Therefore, main fraction of water or NaCl solution could be localized in mesopores and macropores of pretreated silicas. The dispersion media can affect the location of the clusters and domains of water or related solutions in different pores (voids), and NMR cryoporometry allows us to analyze these effects [41].

Stirring of saturated salt solutions or NaCl/water (1:1) mixtures with silicas could result in the formation of salt crystallites because interfacial water is a poorer solvent than bulk one [41]. To determine the sizes of these crystallites (i.e., coherent scattering regions, CSR), X-ray diffraction patterns (Figs. 7a,c and 8) could be treated to analyze the CSR size distributions. More complex size (CSR) distribution functions of NaCl crystallites are observed at lower content of the salt (Fig. 7b,d). It should be noted that evaporation of a fraction of water (the preparation of samples was carried out in air under standard conditions) can enhance the NaCl crystallization before the measurements. This effect could be stronger for the systems with AM-1, since hydrophobic silica more weakly interacts with water (*vide infra* theoretical modeling results), which could form larger domains in larger voids in supra-NP structures.

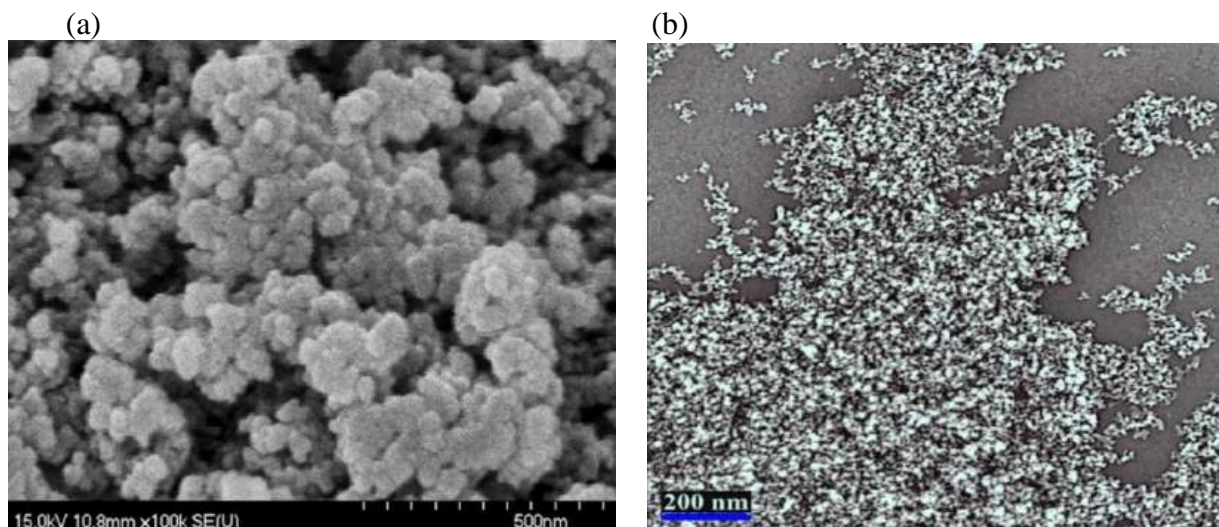


Fig. 3. (a) SEM and (b) TEM images of A-300 showing NPNP aggregates and agglomerates

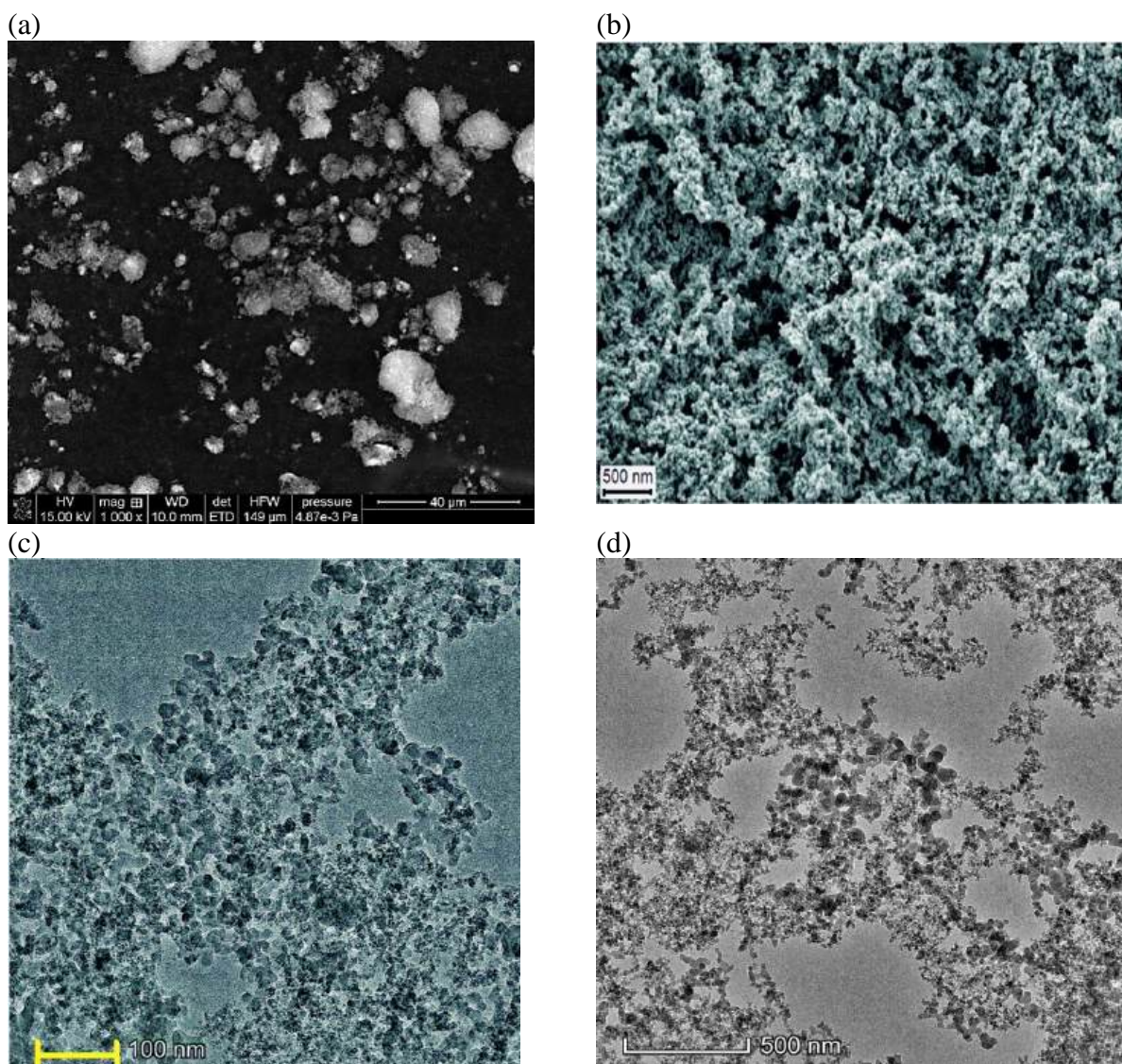


Fig. 4. (a, b) SEM and (c, d) TEM images of AM-1 showing NPNP aggregates and agglomerates

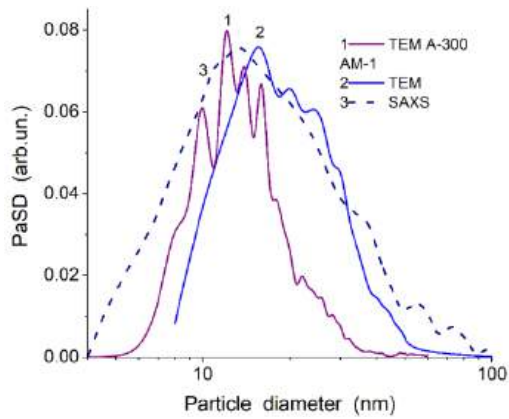


Fig. 5. Particle size distributions of A-300 and AM-1 estimated from TEM images (using ImageJ software, <https://imagej.nih.gov/ij/> with granulometry plugin, <https://imagej.nih.gov/ij/plugins/granulometry.html>) and computed using small angle X-ray scattering (SAXS) data (model of spherical particles [54])

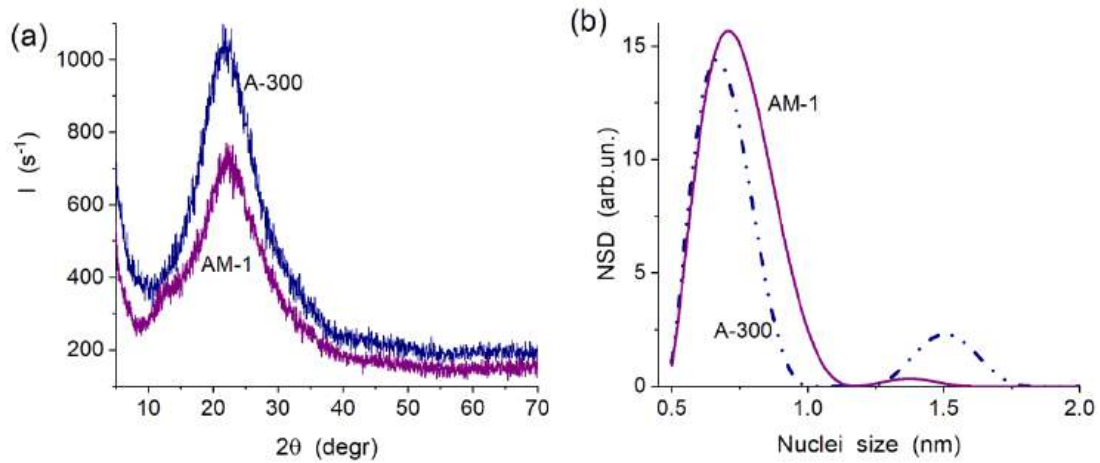


Fig. 6. (a) XRD patterns for initial A-300 and AM-1 and (b) nuclei size distributions (NSD)

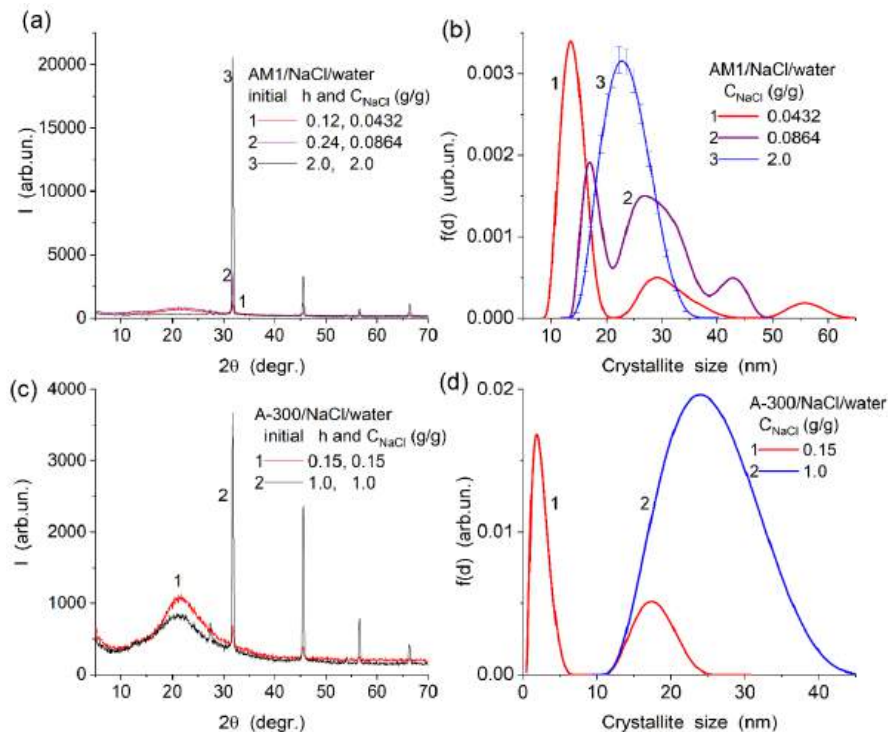


Fig. 7. (a, c) XRD patterns and (b, d) size (CSR) distribution functions for NaCl crystallites bound in wetted (a, b) AM-1 and (c, d) A-300 (initial amounts of water and NaCl content are given in gram per gram of dry silica); in (b) error bars are shown for curve 3 (as a representative example)

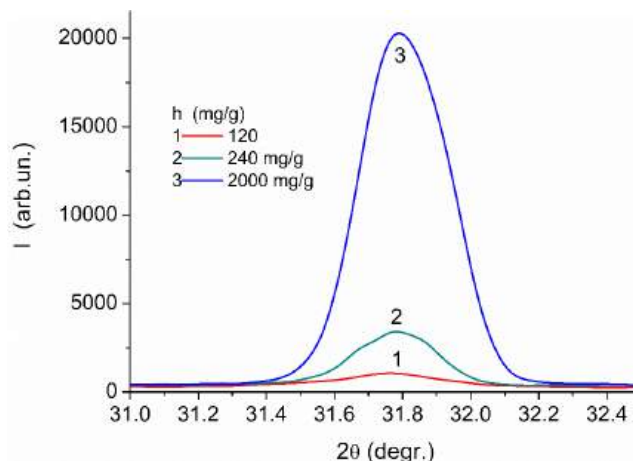


Fig. 8. XRD patterns (main peak of crystalline NaCl) for NaCl/AM-1 differently wetted

Stronger evaporation of water from AM-1 is well seen from the thermogravimetry (TG) data (Fig. 9). For example, the water evaporation from AM-1/NaCl/water at initial $h = 2$ g/g and A-300/NaCl/water at initial $h = 1$ g/g results in similar TG data on removed water at $T < 200$ °C. An increase in the NaCl content (and water amount) results in a shift of the first CSR size peak toward larger sizes of NaCl crystallites (Fig. 7 b,d). The observed changes in the NaCl crystallite sizes dependent on the NaCl content and water amounts could affect the interfacial and temperature behaviors of bound solutions and other characteristics of the systems.

According to the differential thermal analysis (DTA) data (Fig. 9), melting temperature of NaCl crystallites is lower (765 – 793 °C) than that of the bulk salt (801 °C). This effect depends on the NaCl content and silica kind. Subsequent cooling of the samples results in NaCl crystallization at temperatures lower (740–765 °C) than melting one. This effect as well as the melting one depends on the NaCl content and system kind. As a whole, the melting and crystallization temperatures are lower at smaller content of NaCl (due to a difference in the sizes of NaCl particles bound to a silica surface), and the effects are stronger for the systems with hydrophilic A-300. This can be explained by stronger interactions of smaller NaCl crystallites (Fig. 7) with polar silica surface of A-300 composed of smaller NPNP than those of AM-1 (Fig. 5). These effects are observed after water evaporation due to heating upon the TG measurements. The difference in the CSR size distributions (Fig. 7b,d) without sample heating suggests a certain difference in the behavior of the AM-1/NaCl/water and A-300/NaCl/water systems under investigations at room temperature or at $T < T_f$ using various methods (*e.g.*, rheometry, FTIR, ^1H NMR) applied to initially prewetted samples. However, the IR spectra (Figs. 10 and 11) demonstrate that non-strong heating of samples (of very low amounts) by the IR beam during the measurements results in a significant removal of bound water. Despite this effect, residual bound water and NaCl crystallites completely cover the silica surface since the characteristic band of free silanols (at 3750–3740 cm^{-1}) is not observed for the A-300/NaCl/water systems (Fig. 10). For AM-1, the bands related to the C–H stretching vibrations are less sensitive to NaCl/water bound to AM-1 NPNP. However, certain spectral changes are observed for the CH groups in the AM-1/NaCl/water systems since a marked band appears at 2856 cm^{-1} (Fig. 10) in comparison to wetted AM-1 without NaCl (Fig. 11). This suggests that NaCl crystallites are well distributed at a surface not only of A-300 but also AM-1 and can interact with the surface dimethylsilyl groups.

The infrared spectra (Fig. 11) show that mechanical treatment of wetted AM-1 can lead to the appearance of free silanol groups as weak bands $\nu_{(\text{Si})\text{OH}} \approx 3750$ cm^{-1} . Water bound to pretreated AM-1 affects a band at 3680–3660 cm^{-1} related to hardly accessible hydroxyls, and this effect depends on the sample prehistory. Therefore, it could be assumed that water has direct

contact with AM-1 surface patches (siloxane bridges and residual hydroxyls) between the dimethylsilyl (DMS) groups. The area of these patches can be increased during mechanical treatment partially removing the DMS groups. Under pressing of AM-1 at 1300 atm, the DMS functionalities remain (bands at $3000\text{--}2800\text{ cm}^{-1}$); however, the band intensity decreases. The amount of bound water (a broad band at $3600\text{--}3000\text{ cm}^{-1}$) depends on pretreatment conditions and a type of silica. It should be noted that the IR spectra (Fig. 11) are normalized to a band at $1870\text{--}1860\text{ cm}^{-1}$ related the $\equiv\text{Si}\text{--O}\text{--Si}\equiv$ overtone vibrations in NPNP interior and used an internal standard to normalize the amount of sample in the IR beam. Some IR bands non-characteristic for silica and DMS functionalities are due to certain admixtures presented in dimethyldichlorosilane used to modify fumed silica A-200 during the synthesis of AM-1.

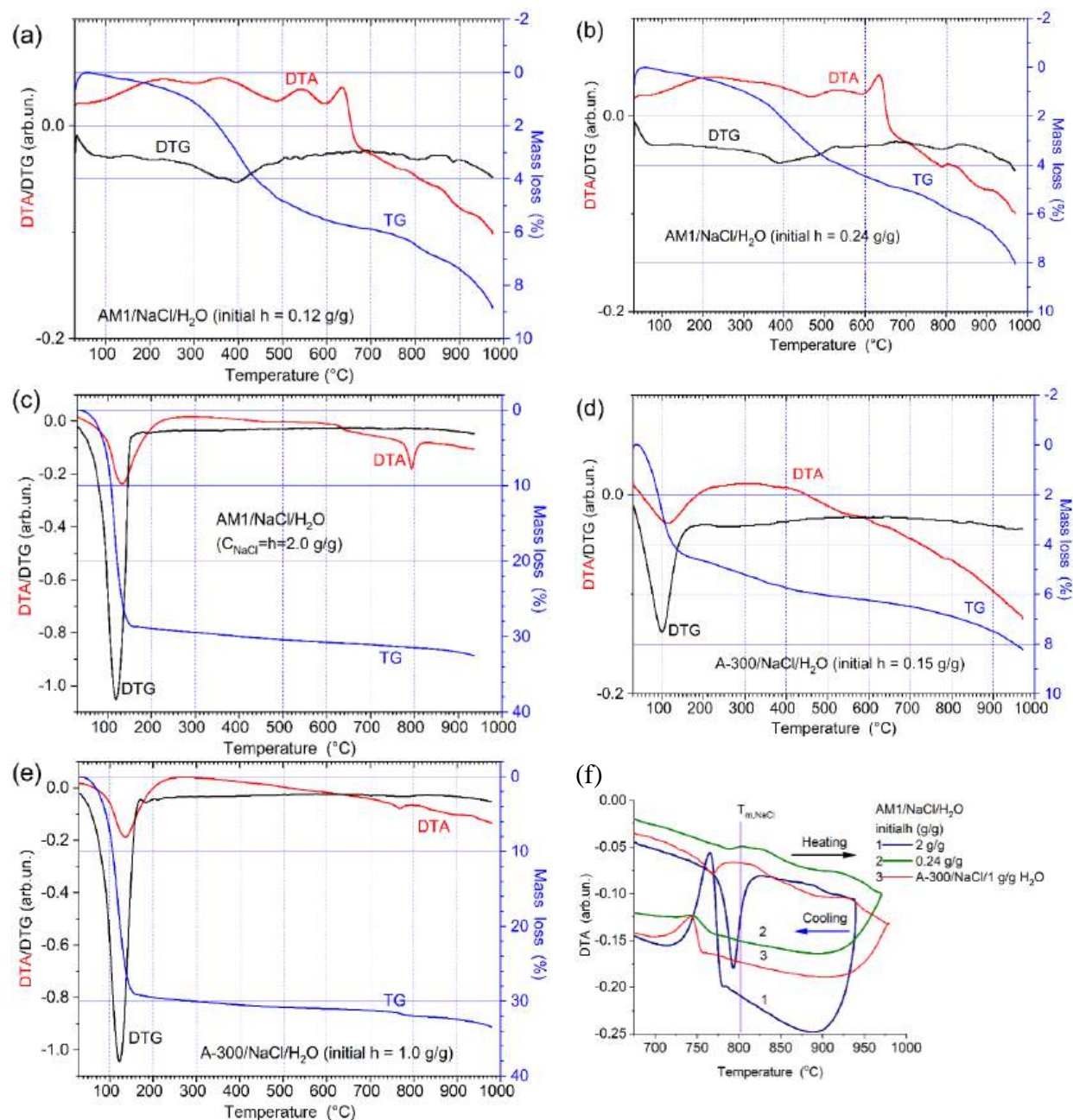


Fig. 9. (a-e) DTA, DTG, and TG curves for studied samples with (a-c) AM-1/NaCl/water and (d, e) A-300/NaCl/water (initial amount of water is shown); (f) DTA curves for heating-cooling of selected samples in the range of 700 – 1000 °C

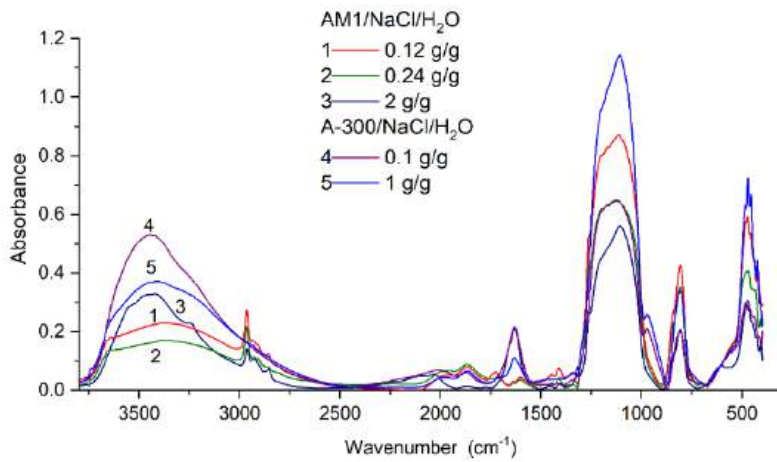


Fig. 10. DRFTIR spectra of nanosilicas with NaCl and bound water (initial water amounts are shown)

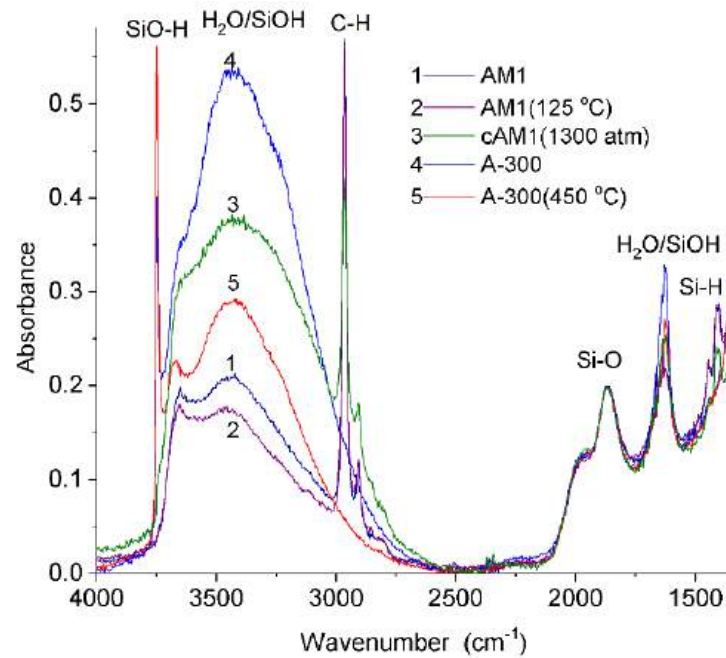


Fig. 11. Infrared spectra of thin pellets (pressed at 1300 or 1500 atm) with AM-1 initial (curve 1), preheated at 125 °C for 2.5 hours (2), compacted with water and pressed into a thin pellet at 1300 atm (3), and A-300 unmodified (4) and preheated at 450 °C for 1 hour (5)

Table 2. Samples under rheometric studies

Silica	NaCl (g/g)	H ₂ O (g/g)
AM-1	0.1	0.1
AM-1	1.0	1.0
AM-1	2.0	2.0
AM-1	-	-
AM-1	-	0.1
AM-1	-	1.0
AM-1	-	2.0
A-300	0.12	0.12
A-300	2.0	2.0
A-300	-	-
A-300	-	0.1
A-300	-	1.0
A-300	-	2.0

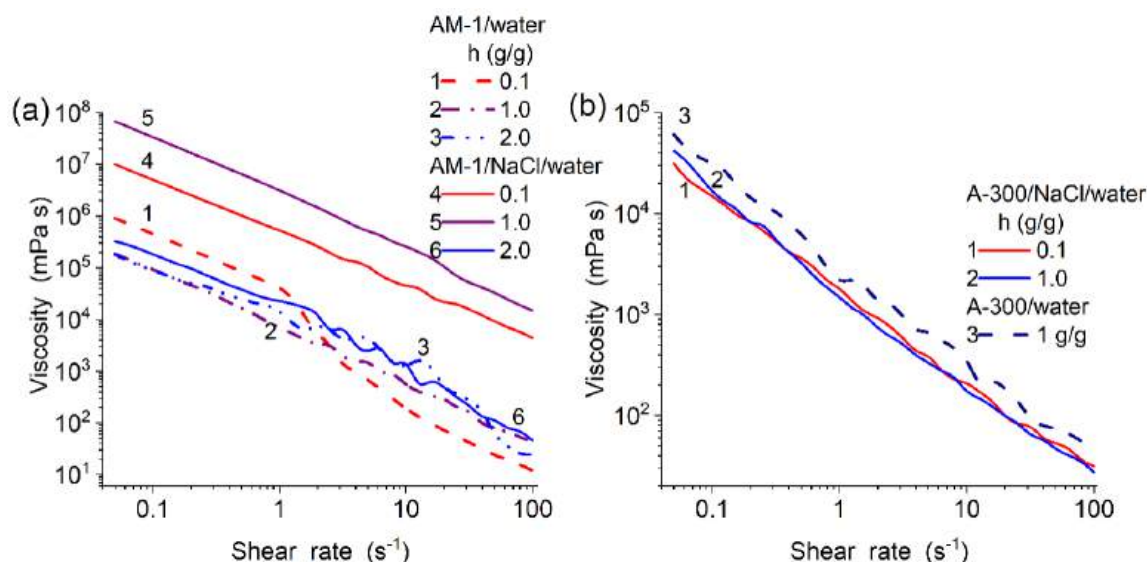


Fig. 12. Viscosity as a function of shear rate for (a) AM-1/water and AM-1/NaCl/water and (b) A-300/water and A-300/NaCl/water at different hydration (NaCl contents are equal to the hydration degree *h*, Table 2)

The rheometric measurements of the wetted AM-1/NaCl and A-300/NaCl (Figs. 12–16, Table 2) show that the viscosity is greater for the hydrophobic AM-1 systems than that based on hydrophilic A-300. The systems with the presence of NaCl are characterized by higher viscosity than that of silica/water (free of NaCl) in the total range of the shear rate range ($\dot{\gamma} = 0.05 - 100 \text{ s}^{-1}$) used. As a whole, these systems demonstrate the pseudo-plastic behavior with the viscosity decreased with increasing shear rate up to 100 s^{-1} . At a minimal content of NaCl bound to AM-1 wetted (Fig. 14b), the storage modulus (related to the stored energy, elastic portion) is higher than the loss modulus (related to the dissipated energy, viscous portion). However, with increasing NaCl content, a contribution of dissipated energy increases at greater shear strain values ($> 10 \%$) (Fig. 13d,f) and it becomes higher than the storage energy. This effect increases and appears at lower shear strain values with increased amounts of bound salt/water. These results could be explained by increasing contribution of larger NaCl crystallites with increasing salt content (Fig. 7b,d). Similar effects are observed for the systems based on hydrophilic A-300 (Fig. 15). However, the difference in the surface structure of silicas plays a certain role (comp. Figs. 13, 15, and 16). The torque vs. shear strain curves show two kinds of the system behavior at lower ($\gamma < 1-2 \%$) and higher ($\gamma > 2-6 \%$) shear strain.

Upon an increase in the shear strain γ , an initial part at $\gamma < 1 - 2 \%$ corresponds to endothermic processes of agglomerate/aggregate decomposition with increasing torque t , and at $\gamma > 2 \%$, the t values decrease with exothermic effects caused by certain rebuilding of the supra-NP structures of different origin. However, in all cases (Figs. 13–15), the reverse branch (with decreasing shear rate from the maximal one) is located below the initial branch (increasing shear rate, strain) since the rebuilding of destroyed supra-NP structures does not reach their levels characteristic for the initial systems with silica/water and silica/NaCl water. Thus, the endothermic effects of breakage of supra-NP structures should be greater than the exothermic ones upon rebuilding new supra-NP structures (mainly due to electrostatic and van-der-Waals binding). The endothermic effects could be analyzed with respect to the activation energy of decomposition of supra-NP structures with increasing share rate. The difference in the system kinds causes certain differences in the distribution functions of the activation energy (AED) of decomposition of interparticle bonds (enhanced breakage of aggregates/agglomerates with increasing $\dot{\gamma}$ value) with increasing shear rate (strain) (Fig. 17). The studied systems are

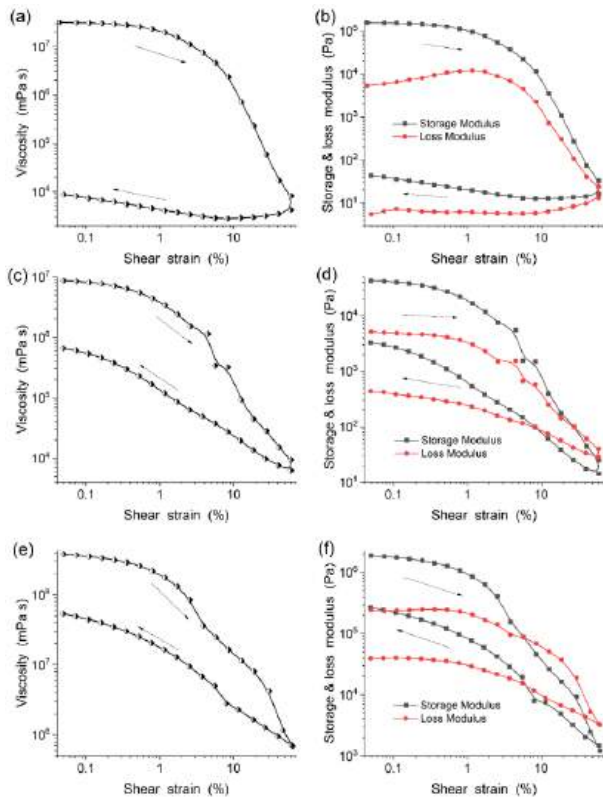


Fig. 13. (a, c, e) Viscosity vs. shear strain and (b, d, f) storage and loss moduli vs. shear strain for AM-1/NaCl/water at $h =$ (a, b) 0.1, (c, d) 1, and (e, f) 2 g/g (NaCl amounts are shown in Table 2)

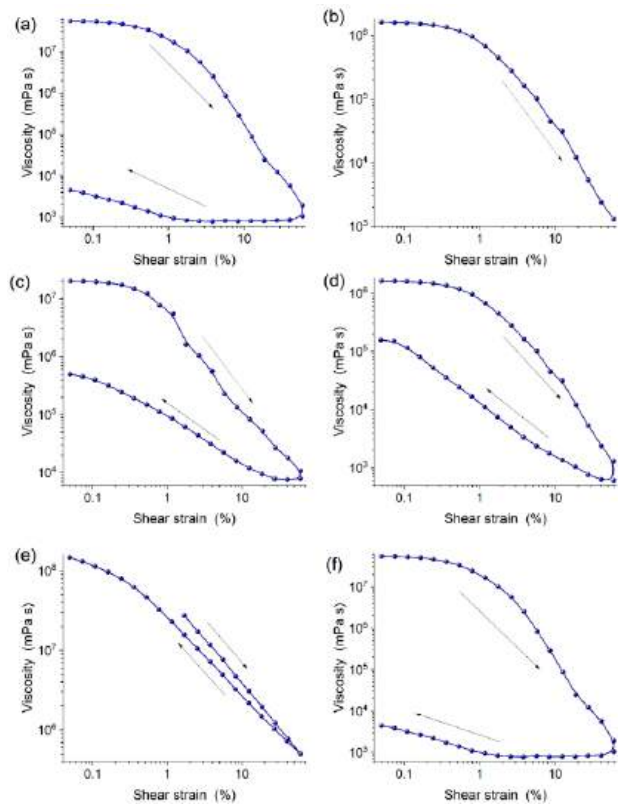


Fig. 14. Viscosity vs. shear strain for (a, c, e) A-300/water, (b, d) A-300/NaCl/water and initial compacted A-300 at $h =$ (a, b) 0.1, (c, d) 1, and (e, f) 2 g/g (NaCl amounts are shown in Table 2)

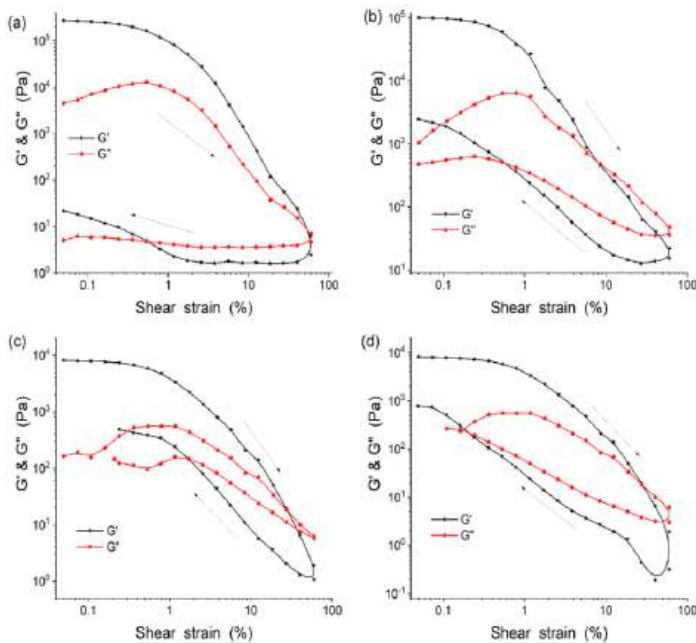


Fig. 15. Storage (G') and loss (G'') moduli vs. shear strain for (a, b) A-300/water and (c, d) A-300/NaCl/water at $h =$ (a, c) 0.1, and (b, d) 1 g/g, and $C_{NaCl} =$ (c) 0.1 and (d) 1 g/g

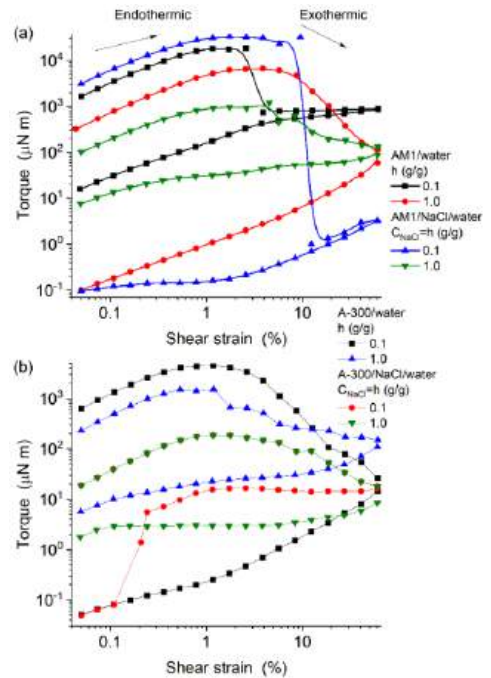


Fig. 16. Torque vs. shear strain for (a) AM-1 and (b) A-300 systems

relatively complex since they include a certain structural hierarchy with silica nanoparticles forming aggregates and agglomerates (Figs. 3–5), various NaCl crystallites (Fig. 7), water domains with various amounts of dissolved NaCl (decreased in water layers closely located to the surface). Therefore, the AED functions could include several peaks (Fig. 17). More rigid structures are decomposed at higher shear rates and need higher activation energy. The highest energy peaks of AED are observed at a minimal content of salt/water, especially for A–300/NaCl/water (Fig. 17c) due to increasing friction between the rheometer disk and sample studied. As a whole, the activation energy (Fig. 17) is greater for the systems based on AM–1 characterized by higher viscosity values (Figs. 12–14). The observed differences in the properties and characteristics of the systems based on AM–1 and A–300 (Figs. 2–17) could appear in the interfacial phenomena studied at low temperatures using ^1H NMR spectroscopy and cryoporometry.

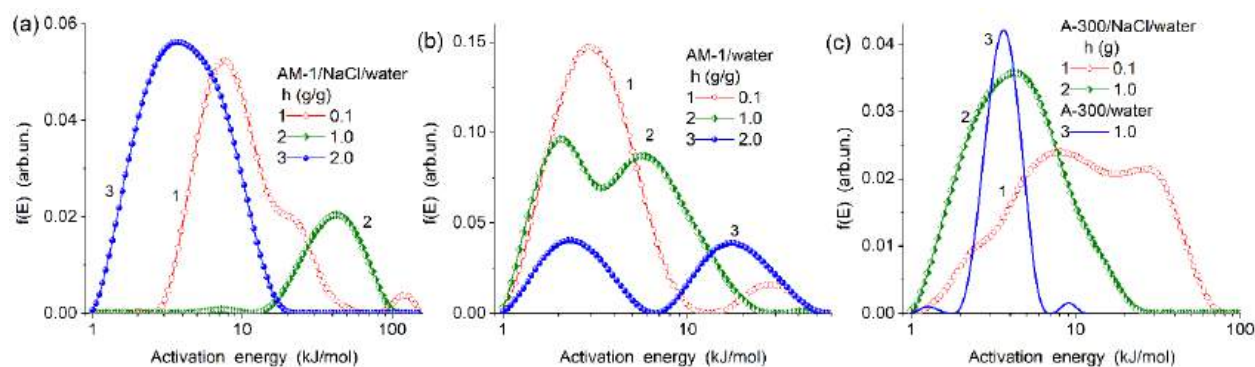


Fig. 17. Activation energy of breakage of interparticle bonds for wetted samples with (a) AM–1/NaCl/water, (b) AM–1/water, and (c) A–300/NaCl/water and A-300/water

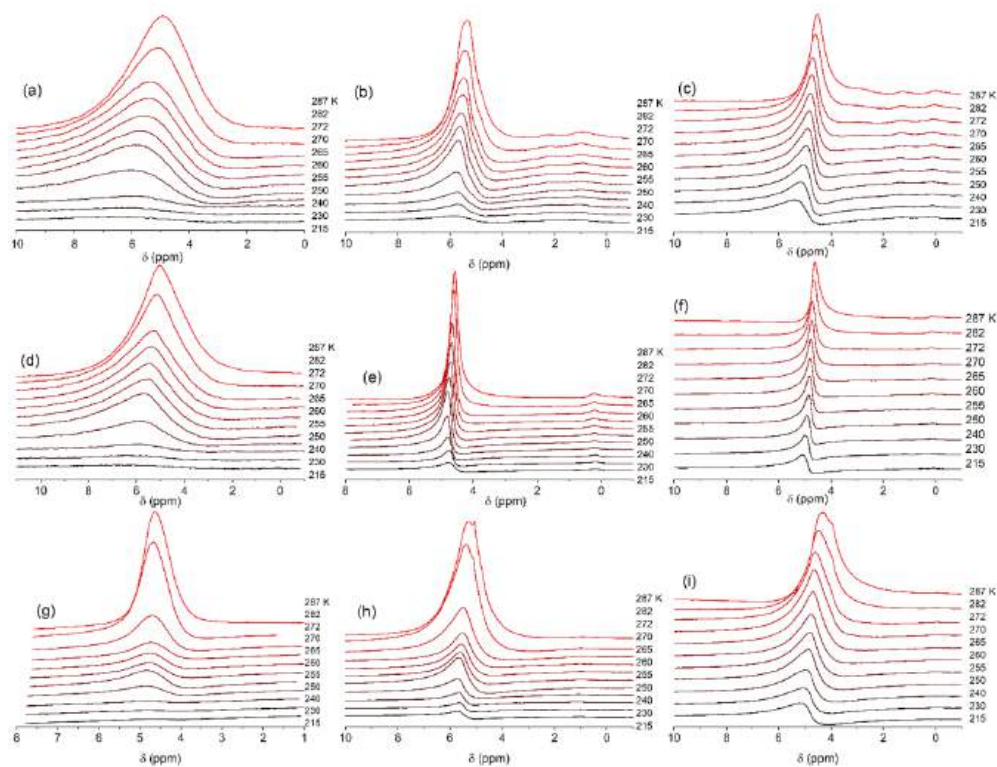


Fig. 18. ^1H NMR spectra of water/NaCl bound AM–1 in (a, d, g) air, (b, e, h) CDCl_3 , and (c, f, i) CDCl_3 (70 %) + CCl_4 (15 %) + DMSO-d_6 (15 %) at $h =$ (a–c) 0.12, (d–f) 0.24, and (g–i) 2.0 mg/g, and $C_{\text{NaCl}} =$ (a–c) 0.043, (d–f) 0.086, and (g–i) 2 g/g (per gram of dry silica)

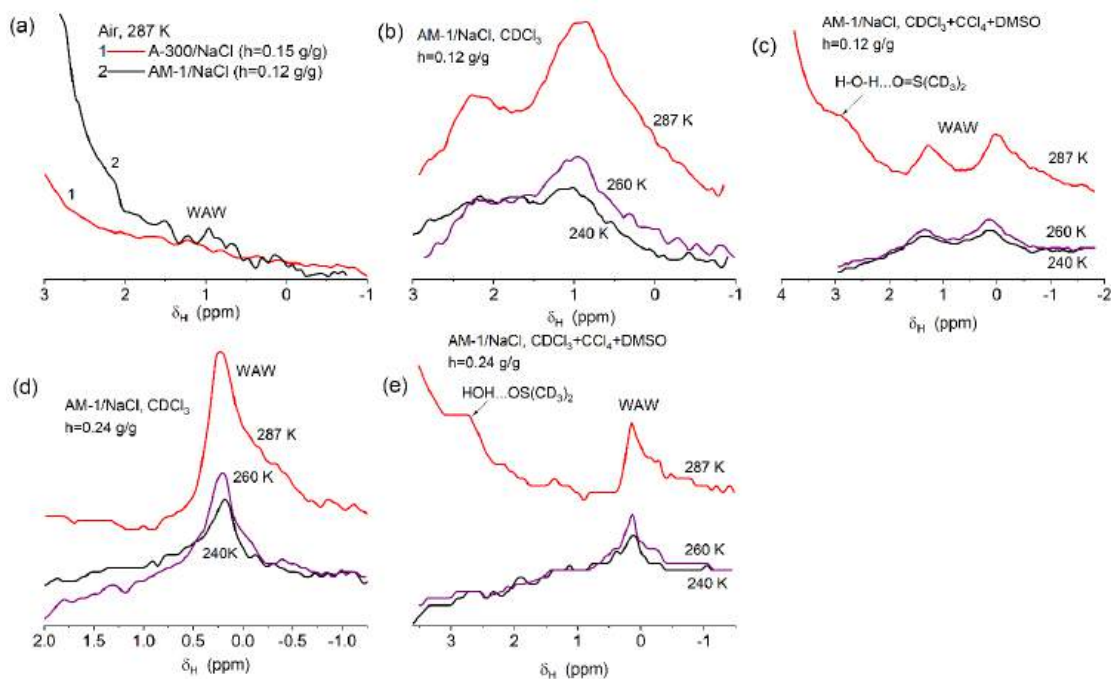


Fig. 19. ^1H NMR spectra (in the range of low δ_{H} values) of water/NaCl bound (a) A-300 and (a-e) AM-1 in (a) air, (b, d) CDCl_3 , and (c, e) $\text{CDCl}_3+\text{CCl}_4+\text{DMSO-d}_6$ at $h =$ (a-c) 0.12 g/g, (d, e) 0.24 g/g

3.2. Interfacial and temperature behaviors of NaCl solutions bound to silicas

For AM-1/NaCl/water (Figs. 18 and 19) and A-300/NaCl/water (Fig. 20) samples located in air and studied using low-temperature ^1H NMR spectroscopy of static samples with increasing temperature from 215 to 287 K, bound water provides a broad signal (of intensity increased with T) at the chemical shift of proton resonance (δ_{H}) corresponding to strongly associated water (SAW) [41] at $\delta_{\text{H}} = 4 - 6$ ppm. These δ_{H} values are because the water HBN structure in SAW is similar to that in liquid bulk water. The signal intensity of unfrozen (at $T < T_f$) water increases with increasing temperature from a certain minimum value corresponding to freezing-out of the most water present in the samples (~ 215 K) to the intensity of completely thawed ice (water at 287 K).

At lower temperatures, there is a downfield shift (δ_{H} increases) and certain asymmetry of the band shape (with a longer wing toward higher δ_{H} values) since more deshielded protons are being in stronger hydrogen bonds in water unfrozen at lower temperatures. AM-1/water/NaCl being in weakly polar deuteriochloroform medium (Fig. 18b,e,h), in addition to the SAW signal, one or two signals appear or become stronger at $\delta_{\text{H}} = 0 - 2$ ppm that could be interpreted as signals of weakly associated water (WAW) (Fig. 19). The molecules in WAW either do not form the hydrogen bonds with other molecules (such as interstitial water molecules) or form 1 - 2 ones per a molecule (with participation both H and O atoms of each molecule in 1D or 2D structures) instead of four hydrogen bonds per a molecule in SAW (3D structures). The maximum WAW signal intensity is observed for a sample containing a minimum amount of water ($h = 0.12$ g/g), which is more strongly clustered. The relative intensity of the WAW signal decreases with increasing AM-1 wetting due to an increase in contribution of SAW (water becomes less clustered). The addition of a polar substance (DMSO) to the dispersion medium (CDCl_3 , $\text{CDCl}_3+\text{CCl}_4$) does not prevent the formation of WAW (Fig. 19c,f,i). However, an additional signal of structures with $\text{H-O-H}\cdots\text{OS}(\text{Me})_2$ appears at $\delta_{\text{H}} = 3$ ppm. It should be noted that WAW is not observed in the A-300/NaCl/water system (Fig. 20) in contrast to the AM-1

systems since the $=\text{Si}(\text{CH}_3)_2$ ‘umbrellas’ strongly enhance the bound water clusterization at a surface of AM-1 (especially at low amounts of water). Thus, even at the presence of the polar component (DMSO) in the dispersion medium, the structure of water clusters and domains in the NaCl solution bound to a surface of silica with bound NaCl crystallites changes slightly. This could be explained by low kosmotropic and chaotropic properties of the Na^+ and Cl^- ions, respectively [1–4], as well as low kosmotropic properties of DMSO.

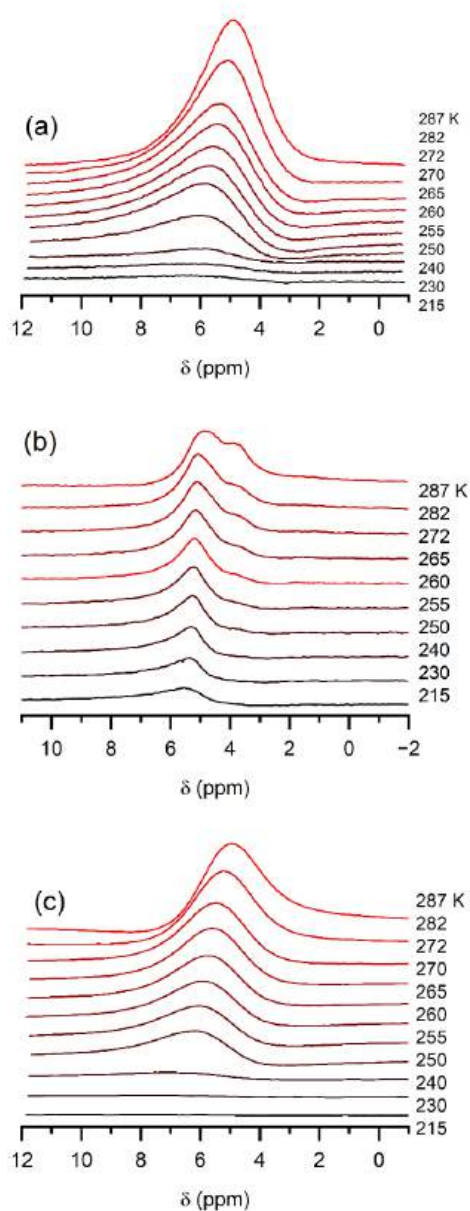


Fig. 20. ^1H NMR spectra of water in the A-300/NaCl/water systems at (a, b) $C_{\text{NaCl}} = h = 0.15$ g/g in (a) air and (b) CDCl_3 , and (c) $C_{\text{NaCl}} = h = 1.0$ g/g in air

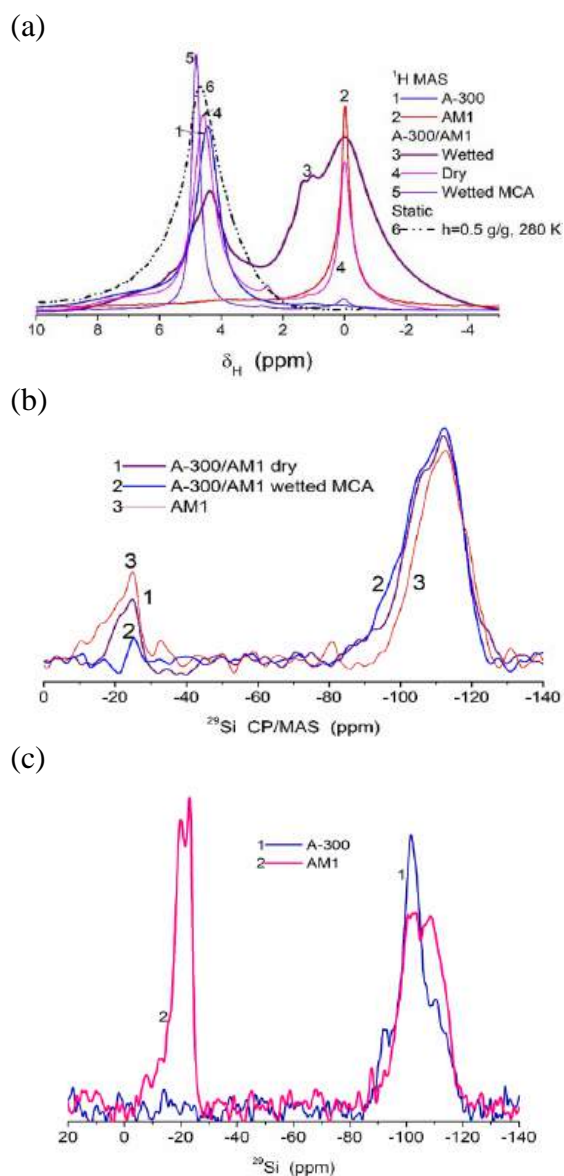


Fig. 21. Solid state NMR spectra of (a) ^1H (MAS, 8 kHz) and (b, c) ^{29}Si (CP/MAS) (Agilent DD2 600 MHz NMR spectrometer) for individual silicas and their blends dry or wetted and treated; (c) air-dry A-300 (curve 1) and AM-1 (2) (rotor frequency 10 kHz)

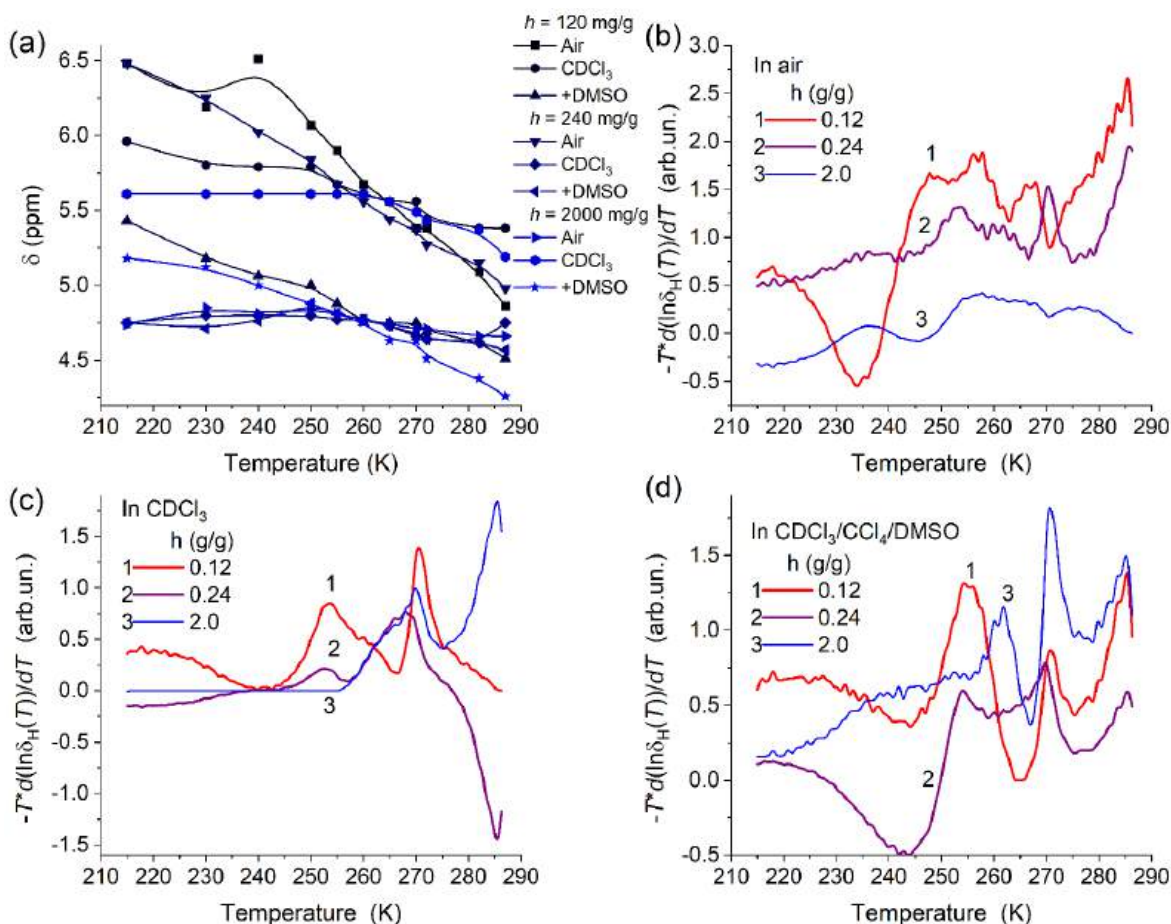


Fig. 22. (a) Chemical shifts vs. temperature for AM-1/NaCl/water systems; and (b-d) functions $s(T) = -T(\partial(\ln\delta(T))/\partial T)_P$ vs. temperature for the systems in different dispersion media (b) air, (c) CDCl_3 , and (d) CDCl_3 (70 %) + CCl_4 (15 %) + DMSO (15 %)

DMSO molecules cannot effectively penetrate into interfacial water clusters since this water is a poor solvent. Possibly, water-DMSO structures are predominantly localized in the dispersion medium phase, *i.e.*, water is dissolved in DMSO, but DMSO is not dissolved in the interfacial water, but DMSO is dissolved in chloroform. This leads to the cryoscopic effects (in addition to CSE) for both DMSO/water and NaCl/water solutions overlapping with CSE. As a whole, the CSE can partially inhibit the cryoscopic effects due to the diminution of solvent activity of bound water [73,74]. However, this inhibition could be smaller for DMSO/water (in the dispersion medium) than for NaCl/water located at the silica surface. This assumption is confirmed by the minimal $\langle T_m \rangle$ values (Table 3) and observation of relatively intensive ^1H NMR signals at 215 K (Fig. 18c,f,i) for the systems containing DMSO addition (due to cryoscopic effects).

For all studied systems based on AM-1, there is a general trend of an increase in the δ_H value with decreasing temperature (Fig. 22a). This could be explained by certain stabilization of more ordered forms of bound water possessing lower mobility at lower temperatures. The absence of linear dependences of δ_H on temperature may be due to the formation of different types of clusters and domains, which include both dissolved and undissolved sodium chloride and water molecules being under different confined space effects and characterized by different cryoscopic effects. Stronger changes in the δ_H values (downfield shift) are observed at a minimal h value for a AM-1/NaCl sample located in air (Fig. 22a). This corresponds to maximal changes (decrease at low T and increase with increasing temperature) in the HBN entropy (Fig. 22b-d). An increase in h (and C_{NaCl}) leads to relatively small changes in the $s(T)$ values vs. T

(Fig. 22b, curve 3). A similar result is for strongly bound water (SBW unfrozen at $T < 260$ K) in AM-1/NaCl/water located in CDCl_3 medium (Fig. 22c). Appearance of DMSO in the dispersion medium affects the temperature behavior of water (Fig. 22d). This is because of transfer of a fraction of water from the interfacial layers into a DMSO fraction. DMSO/water and water could be located in different voids under different confined space effects with addition of the cryoscopic effects for DMSO/water (Fig. 1b) with different changes in their Gibbs free energy (Fig. 1c). The latter is similar to changes in the ΔG values due to interaction of water with a silica surface (Table 3, Fig. 23). Of course, all these effects depend on the water amounts. A minimum of $s(T)$ observed at 245 K is not only at minimal h but also at $h = 0.24$ g/g (due to freezing-out of a fraction of SBW). There are several maxima of $s(T)$ due to melting of frozen SBW (at 245–255 K), weakly bound water (WBW) (at 260–273 K) at different amounts of SAW and WAW, water with delayed melting (kinetically (since heating rate is not small) or due to NaCl crystallization/dissolution effects and release of trapped water) at $T = 273 - 287$ K (Fig. 22 b–d).

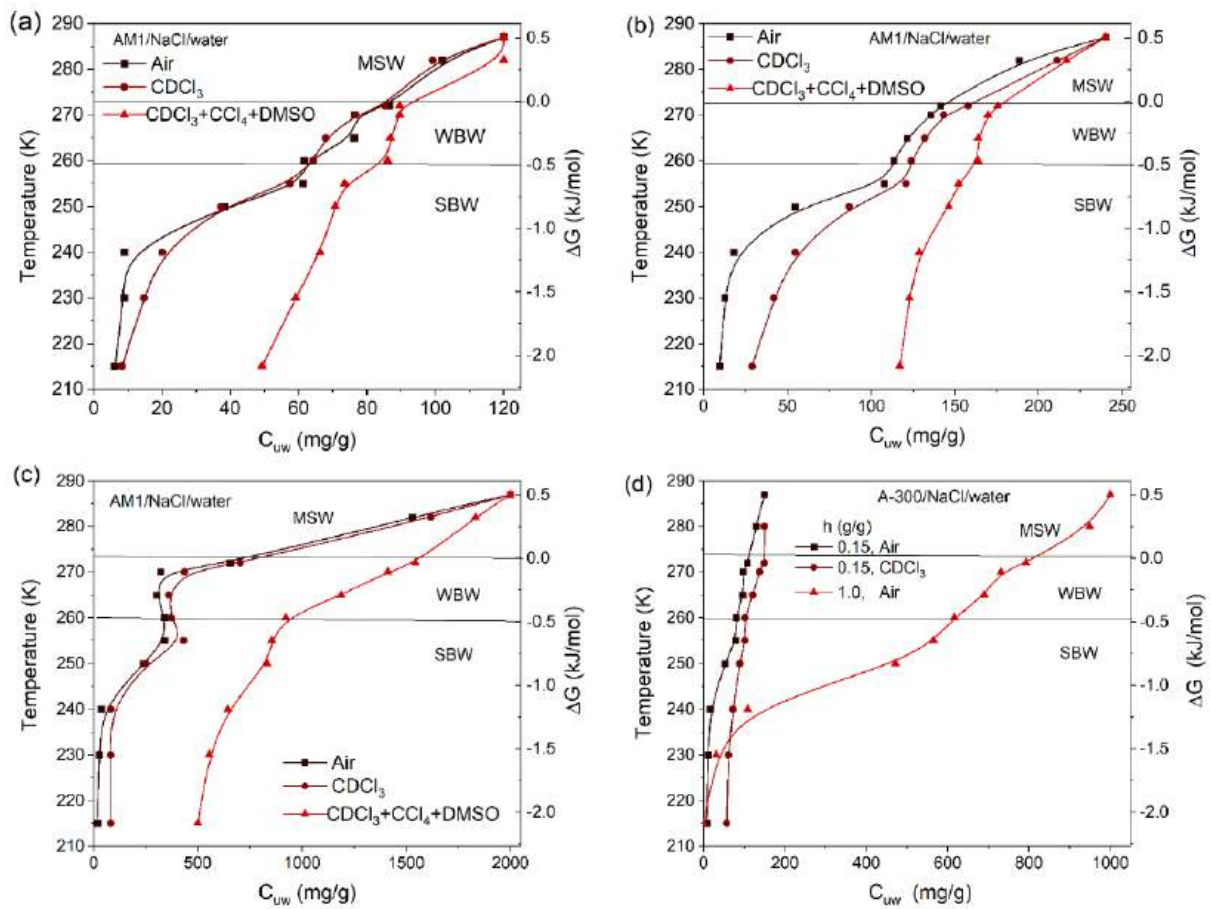


Fig. 23. Unfrozen amounts of water (C_{uw}) vs. temperature and changes in the Gibbs free energy (ΔG) for (a–c) AM-1/NaCl/water and (d) A-300/AM-1/water at $h =$ (a) 0.12, (b) 0.24, (c) 2.0, and (d) 0.15 and 1 g/g

The temperature behavior of bound water is also well observed in curves of C_{uw} vs. T and ΔG vs. C_{uw} (Fig. 23). The amounts of unfrozen water vs. temperature depend on several factors: (i) the freezing point depression (FPD) due to confined space effects since water can be frozen in narrower pores (or voids between nanoparticles) at lower temperatures as described by the Gibbs–Thomson relation for FPD for liquids confined in pores; (ii) cryoscopic effects giving

FPD due to the colligative properties of the solutions of NaCl/water and DMSO/water (Fig. 1); (iii) crystallization and dissolution of NaCl; (iv) changes in the solvent activity and mobility of bound water depending on the confined space effects; and (v) changes in the location of bound water depending on the dispersion media kinds.

Table 3. Characteristics of unfrozen water (WAW and SAW, and WBW and SBW) in aqueous solutions of NaCl (with a fraction of solid NaCl) bound to AM-1 or A-300 in different dispersion media (studied using low-temperature ^1H NMR method)

Sample	Medium	$h(\text{g/g})$	$C_{\text{NaCl}}(\text{g/g})$	$C_{\text{uw}}^{\text{s}}(\text{mg/g})$	$C_{\text{uw}}^{\text{w}}(\text{mg/g})$	$C_{\text{uw}}^{\text{m}}(\text{mg/g})$
A-300	Air	0.15	0.15	80	34	36
A-300	CDCl_3	0.15	0.15	102	43	5
A-300	Air	1.0	1.0	617	203	180
AM-1	Air	0.12	0.0432	62	24	34
AM-1	CDCl_3	0.12	0.0432	64	23	33
AM-1	$\text{CDCl}_3+\text{CCl}_4+\text{DMSO-d}_6$	0.12	0.0432	86	11	23
AM-1	Air	0.24	0.0864	113	32	105
AM-1	CDCl_3	0.24	0.0864	124	38	78
AM-1	$\text{CDCl}_3+\text{CCl}_4+\text{DMSO-d}_6$	0.24	0.0864	164	16	60
AM-1	Air	2.0	2.0	341	398	1.261
AM-1	CDCl_3	2.0	2.0	373	110	1.517
AM-1	$\text{CDCl}_3+\text{CCl}_4+\text{DMSO-d}_6$	2.0	2.0	922	620	458

Continued table 3

Sample	Medium	$-\Delta G_{\text{s}}(\text{kJ/mol})$	$\gamma_{\text{s}}(\text{J/g})$	$\langle T_{\text{m}} \rangle(\text{K})$	$S_{\text{nano,uw}}(\text{m}^2/\text{g})$	$S_{\text{meso,uw}}(\text{m}^2/\text{g})$
A-300	Air	3.00	5.35	246.9	10	12
A-300	CDCl_3	2.94	10.77	233.3	83	11
A-300	Air	2.14	37.40	248.3	0	76
AM-1	Air	2.91	4.07	247.6	7	8
AM-1	CDCl_3	2.73	4.31	246.4	7	7
AM-1	$\text{CDCl}_3+\text{CCl}_4+\text{DMSO-d}_6$	2.90	8.78	220.9	77	7
AM-1	Air	2.75	6.79	248.0	10	17
AM-1	CDCl_3	2.88	9.65	240.2	36	13
AM-1	$\text{CDCl}_3+\text{CCl}_4+\text{DMSO-d}_6$	3.08	18.53	215.0	203	10
AM-1	Air	2.74	20.91	252.1	25	38
AM-1	CDCl_3	2.90	28.27	246.5	131	45
AM-1	$\text{CDCl}_3+\text{CCl}_4+\text{DMSO-d}_6$	2.91	101.24	236.0	0	143

Continued table 3

Sample	Medium	$V_{\text{nano,uw}}(\text{cm}^3/\text{g})$	$V_{\text{meso,uw}}(\text{cm}^3/\text{g})$	$V_{\text{macro,uw}}(\text{cm}^3/\text{g})$
A-300	Air	0.005	0.096	0.049
A-300	CDCl_3	0.038	0.102	0.010
A-300	Air	0	0.757	0.243
AM-1	Air	0.003	0.076	0.041
AM-1	CDCl_3	0.003	0.077	0.040
AM-1	$\text{CDCl}_3+\text{CCl}_4+\text{DMSO-d}_6$	0.034	0.055	0.031
AM-1	Air	0.005	0.131	0.104
AM-1	CDCl_3	0.016	0.132	0.092
AM-1	$\text{CDCl}_3+\text{CCl}_4+\text{DMSO-d}_6$	0.090	0.081	0.069
AM-1	Air	0.011	0.445	1.544
AM-1	CDCl_3	0.059	0.441	1.500
AM-1	$\text{CDCl}_3+\text{CCl}_4+\text{DMSO-d}_6$	0	1.221	0.779

Note. Amounts of samples are *ca.* 0.1 g, medium volume (in an ampoule) is *ca.* 0.9 ml (CDCl_3 or CDCl_3 (70 %) + CCl_4 (15 %) + DMSO (15 %)).

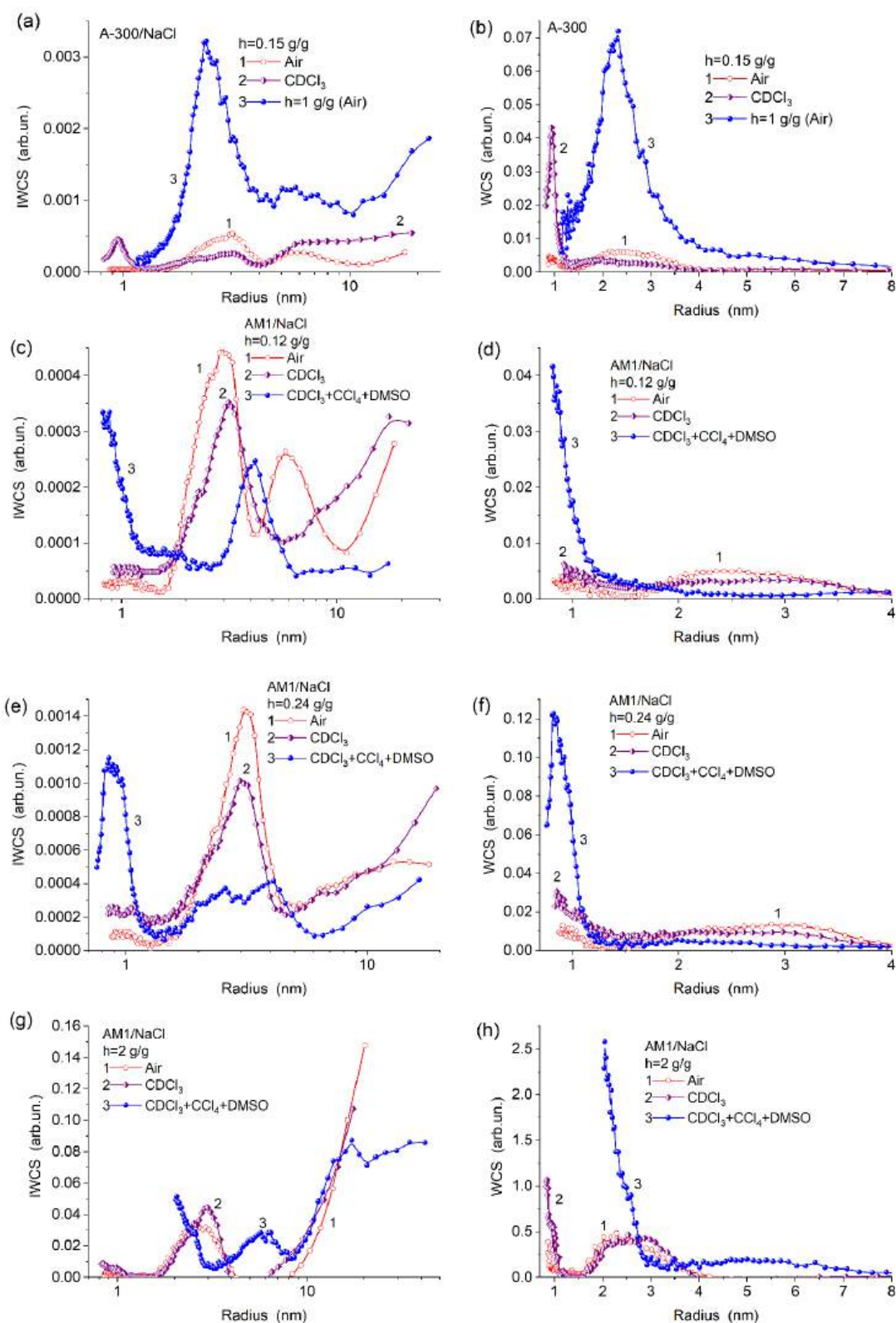


Fig. 24. Unfrozen water cluster size (WCS) distributions (a, c, e, g) incremental and (b, d, f, h) differential for NaCl solutions or solutions with salt crystallites bound to (a, b) A-300 and (c-h) AM-1 at different contents of water/NaCl at $h =$ (a, b) 0.15 and 1.0, (c, d) 0.12, (e, f) 0.24, (g, h) 2 g/g and being in different dispersion media (air, CDCl_3 , $\text{CDCl}_3+\text{CCl}_4+\text{DMSO}$) (NaCl content is shown in Table 3)

Note that all the mentioned effects can differently affect the amounts of SAW, WAW, SBW, and WBW as well as the contributions of SBW and WBW in SAW and WAW. For SBW, the changes in the Gibbs free energy are maximum negative due to adsorption interactions in narrow voids between nanoparticles and in thin surface layers at $|\Delta G| > 0.5$ kJ/mol (Fig. 23). WBW is characterized by negative ΔG at the modulus of $0 < |\Delta G| < 0.5$ kJ/mol. There is a fraction of water giving an increase in C_{uw} at $T > 273$ K (this water could be assigned to metastable water, MSW, C_{uw}^m , Table 3). The appearance of this water is due to delay of melting of WBW/SAW (minor) and changes in NaCl states due to dissolution of crystallites with increasing temperature (since the amount of unfrozen water increases) resulting in release of water trapped in these crystallites. The amounts of water corresponding to each kind can be defined as the concentration of SBW, WBW, and MSW (C_{uw}^s , C_{uw}^w , and C_{uw}^m , respectively, Table 3). The characteristics of these different types of water are summarized in Table 3. Typically, the water amounts located in nanopores (voids) at $R < 1$ nm is relatively small ($V_{nano,uw}$, Table 3, Fig. 24) and depends on the water/NaCl amounts and dispersion media kind. The presence of $CDCl_3$ leads to an increase in this fraction of water (especially, for the A-300 systems, Fig. 24a,b) because chloroform can displace water into narrow pores inaccessible for larger $CDCl_3$ molecules than H_2O or into broader pores (Fig. 24) [41]. Both displacements result in a decrease in the contact area between immiscible liquids. The main fraction of unfrozen bound water is located in mesopores (Table 3, $V_{meso,uw}$) and macropores ($V_{macro,uw}$) (Fig. 24). However, the main contribution into the surface area in contact with unfrozen water (Table 3, $S_{nano,uw}$ and $S_{meso,uw}$) is due to water located in nanopores.

The average value of melting temperature of frozen water (Table 3, $\langle T_m \rangle$) is minimal with the presence of DMSO in the dispersion media due to the strong cryoscopic effect observed for the DMSO/water mixtures, especially at C_{DMSO} 50 – 70 % (Fig. 1b). These systems are characterized by maximal γ_s values (showing the modulus of total changes in the Gibbs free energy due to interactions of water with surroundings) as well as maximum values of C_{uw}^s and $|\Delta G_s|$ (related to SBW). It should be noted that the $CDCl_3$ (without DMSO) effects more strongly depend on the amounts of water (Table 3, Figs. 23 and 24). The colligative properties of NaCl/water results in a specific effect, which is better seen at $h = C_{NaCl} = 2$ g/g (Fig. 23c), when C_{uw} is practically constant at $T = 255$ – 270 K (air and $CDCl_3$ dispersion media). These systems are characterized by zero contribution of bound water in clusters/domains of small sizes at $R < 2$ nm (WCS, Fig. 24 g, h).

It should be noted that the C_{uw}^m value (Table 3) may depend on various experimental conditions (*e.g.*, heating rate, C_{NaCl} , h). However, the MSW amount depends mainly on the lifetime of the metastable NaCl crystallites transforming into the solution at $T > 273$ K. Here MSW was observed during 15 min.

Theoretical modeling (Figs. 25–32, Tables 4 and 5) shows that NaCl dissolved or undissolved non-strongly affects the characteristics of bound water. This is in agreement with low kosmotropic and chaotropic properties of the Na^+ and Cl^- ions, respectively [1–4]. The experimental 1H NMR spectra are simpler (and narrower) than theoretical ones due to the differences in the model and real systems (with respect to particle sizes (Fig. 25), amounts and location of water, sizes of its clusters and domains, temperature effects, proton-exchange reactions, *etc.*). However, theoretical modeling gives correct (both qualitatively and quantitatively) changes in the systems based on hydrophobic and hydrophilic silicas. First, it shows the WAW appearance at a surface of AM-1. Second, the interaction energy of water with hydrophobic silica is lower than that for hydrophilic one (Tables 4 and 5), and the effects of a silica surface strongly decrease for distant water layers. Third, the probability of dissociation of water molecules at a surface of AM-1 is lower than that at a surface of hydrophilic silica where Eigen (H_3O^+) and Zundel ($H_5O_2^+$) cations appear (Fig. 26) that affect the temperature and interfacial behaviors of bound water. However, in the case of the interaction of water molecules

with residual silanols at a surface of AM-1, the Eigen and Zundel cations could appear (Fig. 26b). Fourth, the water clusterization increases with decreasing amounts of water and this effect is much stronger for AM-1 than for hydrophilic silica (Figs. 26–31), and it is enhanced by chloroform (as dispersion medium) providing increasing contribution of WAW (Fig. 28). Sixth, the presence of dissolved or undissolved NaCl weakly affects the chemical shifts of bound water (Fig. 29–31).

For dimethylsilyl-modified silica, the Gibbs free energy of solvation in water is negative for completely hydrophobized surface (in contrast to silica completely modified by, *e.g.*, trimethylsilyl groups), despite its increases with increasing degree of the surface hydrophobization (Fig. 32). This explains (i) the possibility of wetting and completely sinking of compacted AM-1 in bulk water; and (ii) certain effects observed upon rheometric measurements, *e.g.*, two types of relationships between the torque and shear strain as well as between the storage and loss moduli and shear strain.

Table 4. QC computation results on water interaction with hydrophobic and hydrophilic silicas (methods: PM7 and DFTB+)

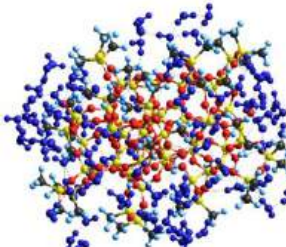
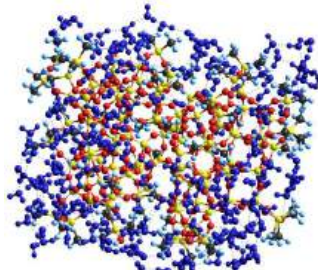
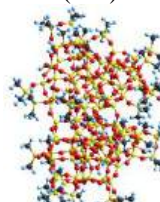
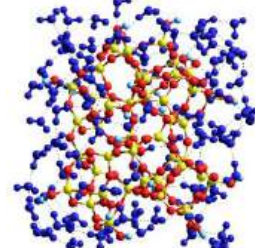
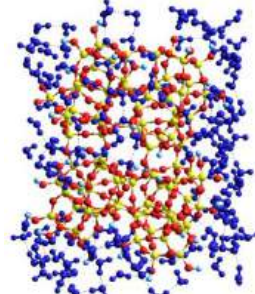
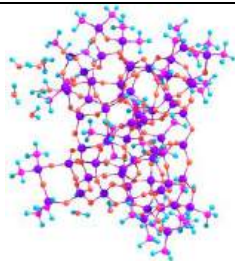
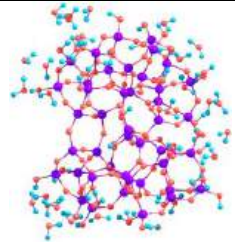
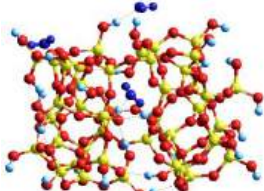
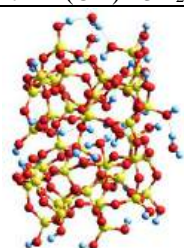
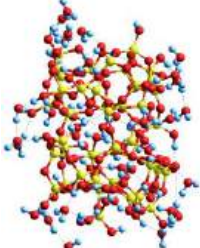
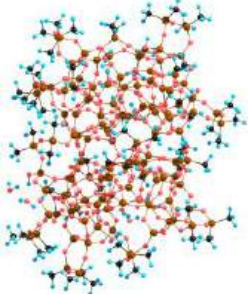
System	Interaction energy per one water molecule E_{1w} (kJ/mol)	
	PM7	DFTB+
	-27.4 (95 H ₂ O) -48.6 (45 H ₂ O) Cluster (SiO _{4/2}) ₄₄ (OH) ₃ (Si(CH ₃) ₂) ₂₁	-10.0 (95 H ₂ O)
	-19.9 (213 H ₂ O) -33.6 (104 H ₂ O) Cluster AM-1 (SiO _{4/2}) ₈₈ with 8(OH) + 31(Si(CH ₃) ₂) 	-6.0 (213 H ₂ O)
	-25.4 (96 H ₂ O) -37.2 (50 H ₂ O) Cluster (SiO _{4/2}) ₄₄ with 24(OH)	
	-25.7 (137 H ₂ O) -39.5 (70 H ₂ O) Cluster (SiO _{4/2}) ₈₈ with 40 OH 	-12.8 (125 H ₂ O)

Table 5. DFT (ω B97X-D/cc-pVDZ) computation results on water interaction with hydrophobic and hydrophilic silicas

System	Interaction energy per one water molecule E_{1w} (kJ/mol)
 <p>(SiO_{4/2})₄₄ with 3(OH) + 21(Si(CH₃)₂) and bound 9H₂O</p>	<p>–49.2 kJ/mol per 1 H₂O (with consideration of interactions between water molecules) –29.0 kJ/mol per 1 H₂O between cluster and shell</p>
 <p>(SiO_{4/2})₄₄ with 24(OH) and bound 40 H₂O</p>	<p>–78.2 kJ/mol per 1 H₂O between cluster and shell (H⁺ transfer from silica toward water shell)</p>
 <p>Defect in cluster volume (Si₄₃O₁₀₀H₂₈): 4H replace Si in (SiO_{4/2})₄₄ with 24(OH) +3H₂O</p>	<p>+ 3H₂O –62.1 kJ/mol per 1 H₂O between cluster and shell (–62.5 kJ/mol with consideration of interactions between water molecules) +4H₂O Silica – water shell (with no H⁺ transfer) and 1 H₂O is intraparticle molecule –76.8 kJ/mol</p>
	<p>+8 H₂O –90.2 kJ/mol</p> <p>11 H₂O –76.4 kJ/mol</p> <p>22 H₂O –57.2 kJ/mol</p>
	<p>42 H₂O –51.0 kJ/mol</p>
 <p>Cluster AM–1 (SiO_{4/2})₈₈ with 8(OH) + 31(Si(CH₃)₂)</p>	<p>10H₂O –108.7 kJ/mol</p>

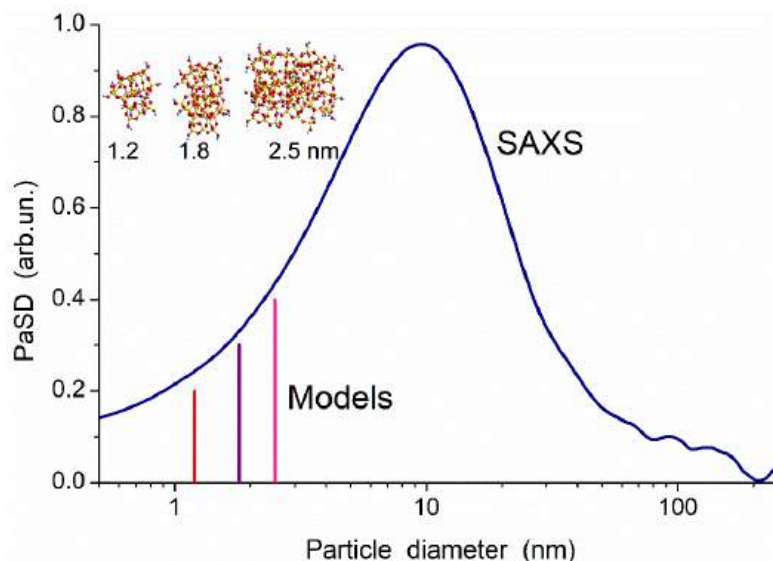


Fig. 25. Particle size distribution of initial A-300 powder according to small angle X-ray scattering (SAXS) data and sizes of some silica clusters (with 22, 44, and 88 $\text{SiO}_{4/2}$ tetrahedrons) used in quantum chemical calculations

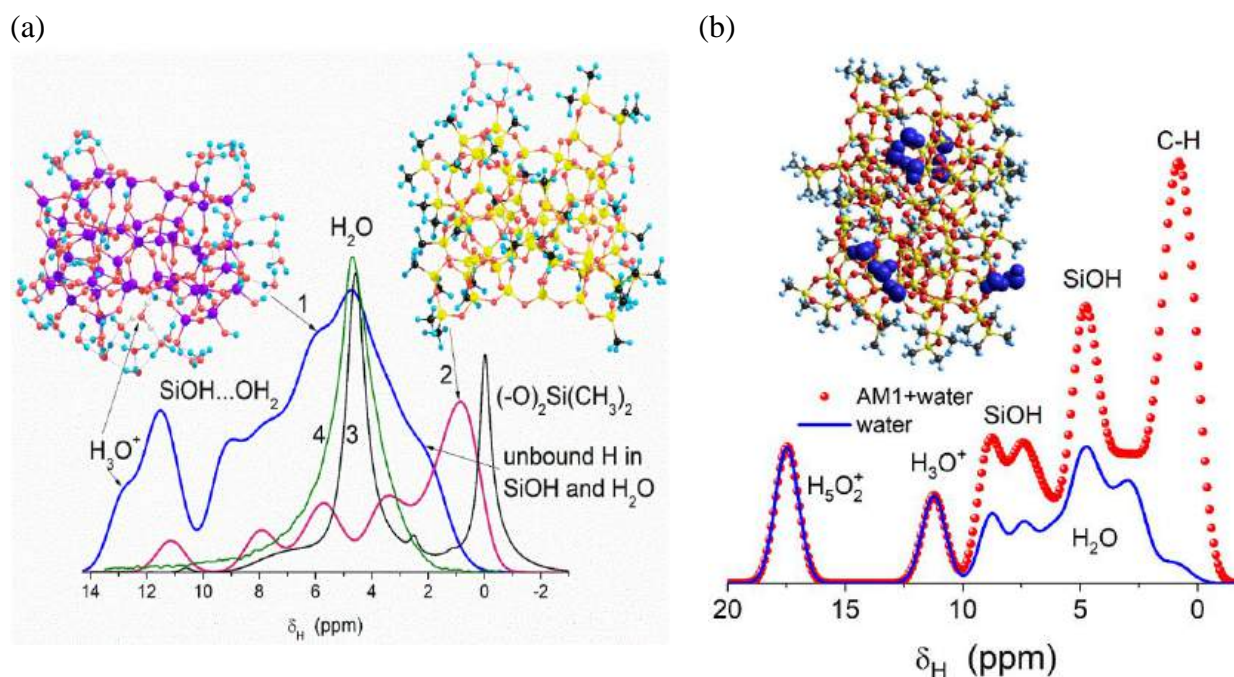


Fig. 26. Theoretical (GIAO/ ω B97X-D/cc-pVDZ) ^1H NMR spectra of water (molecules and ions) bound to (a) hydrophilic (curve 1, 44 $\text{SiO}_{4/2}$ tetrahedrons + 43 H_2O) and hydrophobic AM-1 (curve 2, 44 $\text{SiO}_{4/2}$ + 19 $\text{Si}(\text{CH}_3)_2$ + 9 H_2O) silica clusters, as well ^1H lines linked to the $\equiv\text{SiOH}$ and $(-\text{O})_2\text{Si}(\text{CH}_3)_2$ groups; and experimental ^1H MAS (curve 3) and static (curve 4) NMR spectra of A-300/AM-1 (1/1) blend (note that the surface SiOH and $(-\text{O})_2\text{Si}(\text{CH}_3)_2$ groups in A-300 and AM-1, respectively, do not contribute the spectrum (4) of the static samples), and (b) weakly wetted AM-1 modelled by $(\text{SiO}_{4/2})_{88}$ with 8(OH) + 31($\text{Si}(\text{CH}_3)_2$) + 10 H_2O (Table 4, last row)

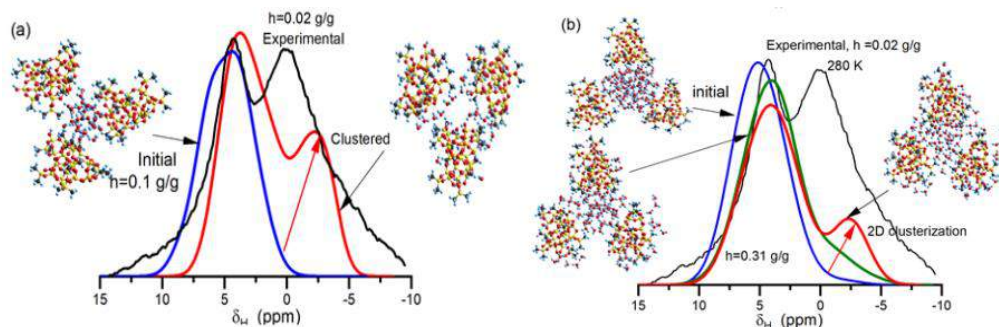


Fig. 27. Theoretical (PM7 with correlation function of δ_H vs. q_H based on DFT ω B97X-D/cc-pVDZ and PM7 calculations) ^1H NMR spectra of water bound in a void between three particles of AM-1 at different distributions of water in larger and smaller cluster at $h =$ (a) 0.1 g/g and (b) 0.31 g/g (experimental curve corresponds to AM-1 at low hydration)

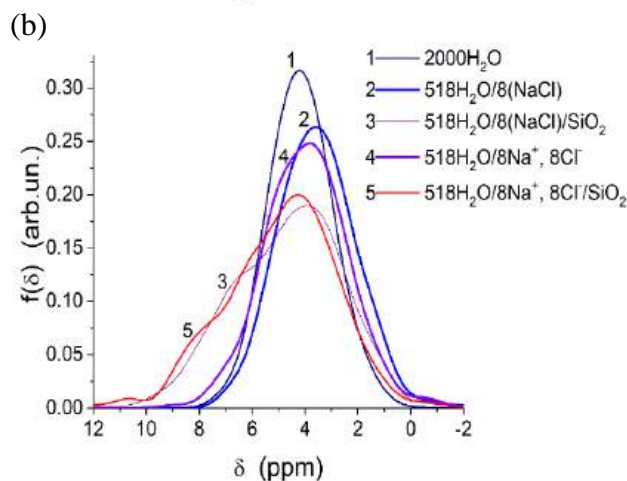
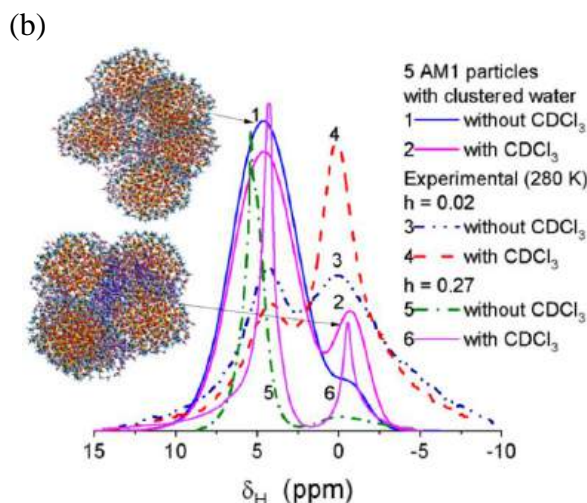
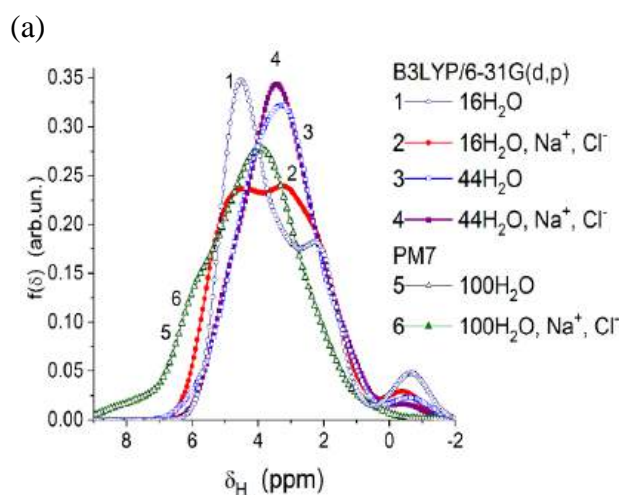
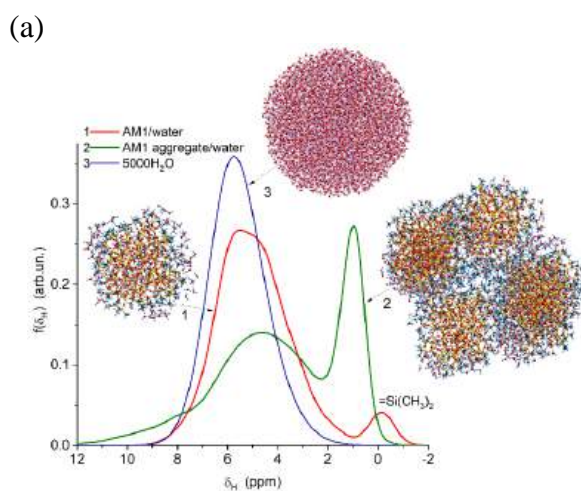


Fig. 28. Theoretical ^1H NMR spectra of water (a) alone and bound to AM-1 nanoparticles and (b) bound in voids between five AM-1 particles (at $h = 0.2$ g/g) without (curve 1) or with CDCl_3 (2); experimental curves (curves 3–6) corresponding to treated AM-1 at lower (0.02 g/g, curves 3 and 4) and higher (0.27 g/g, curves 5 and 6) hydration without (3, 5) or with the presence of CDCl_3 (4, 6)

Fig. 29. Theoretical ^1H NMR spectra of (a) water clusters alone and with Na^+ and Cl^- ions (DFT and PM7) and (b) water clusters alone or with undissolved or dissolved NaCl alone or bound to silica cluster (PM7 method)

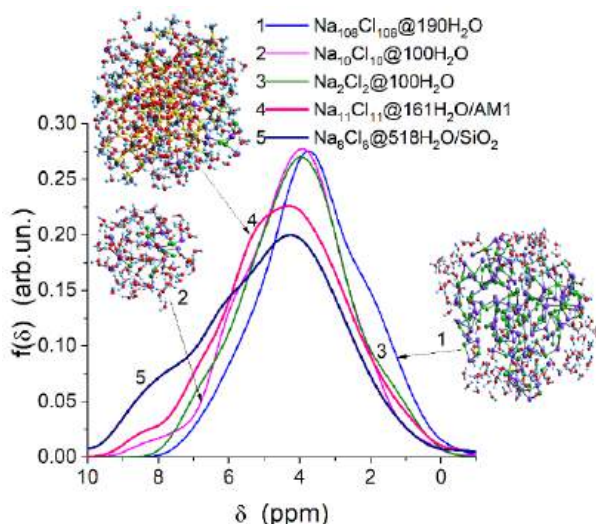


Fig. 30. Theoretical ^1H NMR spectra of water/NaCl (curves 1–3) with undissolved NaCl (1) or dissolved NaCl (2, 3) or NaCl dissolved in water bound to AM–1 (4) or A–300 (5)

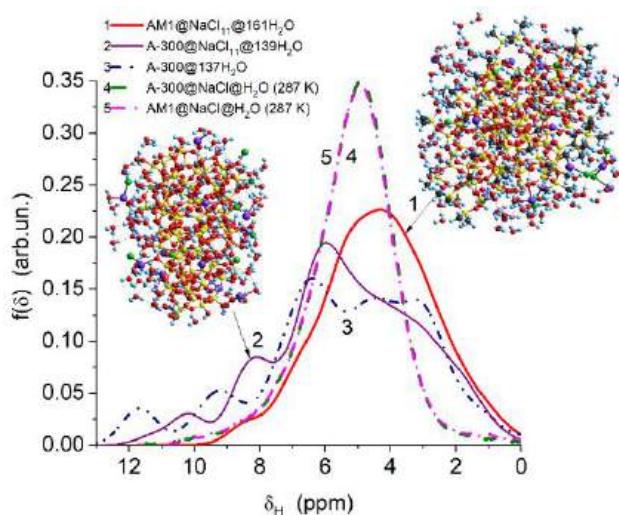


Fig. 31. Theoretical and experimental ^1H NMR spectra for systems based on wetted AM–1/NaCl and A–300/NaCl

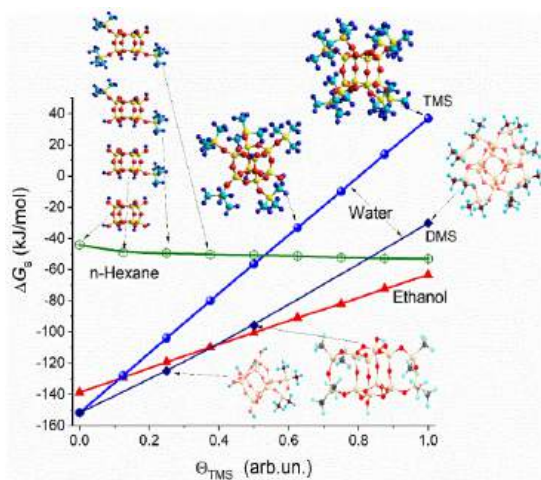


Fig. 32. Gibbs free energy of solvation vs. a number of trimethylsilyl (TMS) and dimethylsilyl (DMS) groups in silica clusters $\text{Si}_8\text{O}_{12}(\text{OH})_n(\text{OSi}(\text{CH}_3)_3)_{8-n}$ ($n = 8, 7, 6, \dots, 0$) calculated using SMD/ ω B97X–D/cc–pVDZ//cc–pVDZ for water (TMS and DMS), ethanol, and *n*-hexane (TMS) as solvents

CONCLUSION

Water alone and concentrated aqueous solutions of NaCl can be easily introduced into interparticle voids not only of hydrophilic fumed silica A–300 but also hydrophobic fumed silica AM–1 by simple stirring of the blends in a porcelain mortar using pretreated compacted silicas. This explains by relatively low hydrophobicity of AM–1 containing pair-crosslinked dimethylsilyl groups (these short hydrophobic ‘umbrellas’ cannot provide complete coverage of the surface) and residual silanols at a surface. Both NaCl (including solution and crystallites) and water are relatively uniformly distributed in interparticle voids of the supra-NP structures of both silicas.

In air, water alone or clustered salt solutions (SAW fraction) bound to fumed silicas (compacted to reduce the effects of residual air microbubbles) have a structure similar to that of liquid water because the Na^+ and Cl^- ions are weakly kosmotropic and chaotropic, respectively. In weakly polar CDCl_3 dispersion medium, in addition to the ^1H NMR signal of strongly associated water, one or two signals of WAW clustered with partially broken HBN are observed in the spectra of wetted AM–1/NaCl. However, WAW is not observed for wetted A–300/NaCl,

but ^1H NMR signals of SAW become more complex with maxima at *ca.* 6 and 4 ppm. This difference could be explained by the effects of AM-1 surface $(-\text{O})_2\text{Si}(\text{CH}_3)_2$ functionalities enhancing the clusterization of bound water. As a whole, the difference in the surface nature of AM-1 and A-300 affects: (i) the NaCl crystallite size (CSR) distributions according to the XRD data; (ii) melting/crystallization temperatures of NaCl (TG/DTA data); (iii) viscosity/shear rate (shear strain), storage/loss moduli and torque *vs.* shear strain relationships, distribution functions of the activation energy of breakage of supra-NP structures (rheometric data); (iv) temperature and interfacial behaviors of water alone and NaCl solutions in the temperature range of 215–287 K, appearance of unfrozen (immobile) water at $T > 273$ K due to NaCl effects (*i.e.*, at $273 \text{ K} < T < 287 \text{ K}$, a fraction of the salt solution can be in a metastable state (MSW), characterized by the coexistence of solid and liquid phases, and the amount of MSW increases with increasing hydration and NaCl content according to low-temperature ^1H NMR spectroscopy of static samples); (v) changes in the dispersion media (air, hydrophobic CDCl_3 , mixture with $\text{CDCl}_3/\text{CCl}_4/\text{DMSO}$) strongly affect the behavior of water alone and NaCl/water because they force the changes in the location of the solution and affect related confined space effects as well the cryoscopic effects observed for the solutions of NaCl/water and water/DMSO.

The analyzed phenomena are of interest from both theoretical and practical points of view, since their consideration allows one to better understand and control the characteristics and properties of composites based on hydrophilic and hydrophobic fumed silicas used, *e.g.*, with solutions of various salts, solutes, and co-solvents.

REFERENCES

1. Ickes L., Welti A., Hoose C., Lohmann U. Classical nucleation theory of homogeneous freezing of water: thermodynamic and kinetic parameters. *Phys. Chem. Chem. Phys.* 2015. **17**: 5514.
2. Chaplin M. *Water structure and science*. <http://www1.lsbu.ac.uk/water/>, accessed on 14 September, 2024.
3. Mancinelli R., Botti A., Bruni F., Ricci M. A. Hydration of sodium, potassium, and chloride ions in solution and the concept of structure maker/breaker. *J. Phys. Chem. B.* 2007. **111**: 13570.
4. Sahle C.J., de Clermont Gallerande E., Niskanen J., Longo A., Elbers M., Schroer M.A., Sternemann C., Jahn S. Hydration in aqueous NaCl. *Phys. Chem. Chem. Phys.* 2022. **24**: 16075.
5. Shultz M.J., Gubbins E.F., Davies R.G., Lin Z., Xiong Z. Ice interfaces: vapor, liquid, and solutions. *J. Phys. Chem. C.* 2024. **128**(30): 12326.
6. Zhou K., Qian C., Liu Y. Quantifying the structure of water and hydrated monovalent ions by density functional theory-based molecular dynamics. *J. Phys. Chem. B.* 2022. **126**(49): 10471.
7. Zhuang D., Riera M., Zhou R., Deary A., Paesani F. Hydration structure of Na^+ and K^+ ions in solution predicted by data-driven many-body potentials. *J. Phys. Chem. B.* 2022. **126**(45): 9349.
8. Ho T.H., Do T.H., Tong H.D., Meijer E.J., Trinh T.T. The role of chloride ion in the silicate condensation reaction from ab initio molecular dynamics simulations. *J. Phys. Chem. B.* 2023. **127**(36): 7748.
9. Luo P., Zhai Y., Senses E., Mamontov E., Xu G., Y Z, Faraone A. Influence of kosmotrope and chaotrope salts on water structural relaxation. *J. Phys. Chem. Lett.* 2020. **11**(21): 8970.
10. Bodnar R.J. Revised equation and table for determining the freezing point depression of H_2O -NaCl solutions. *Geochim. Cosmochim. Acta.* 1993. **57**: 683.

11. Conde M.M., Rovere M., Gallo P. Molecular dynamics simulations of freezing-point depression of TIP4P/2005 water in solution with NaCl. *J. Mol. Liquids*. 2018. **261**: 513.
12. Hewage S.A., Tang C.-S., Mehta Y., Zhu C. Investigating cracking behavior of saline clayey soil under cyclic freezing-thawing effects. *Engineering Geology*. 2023. **326**: 107319.
13. Ketcham S.A., Minsk L.D., Blackburn R.R., Fleege E.J. *Manual of practice for an effective anti-icing program. A guide for highway winter maintenance personnel*. (US Army Cold Regions Research and Engineering Laboratory Corps of Engineers: Hanover, New Hampshire, 1996. <https://www.fhwa.dot.gov/publications/research/safety/95202/index.cfm>.)
14. Gupta S., Pel L., Kopinga K. Crystallization behavior of NaCl droplet during repeated crystallization and dissolution cycles: An NMR study. *J. Crystal Growth*. 2014. **391**: 64.
15. Yamaguchi T., Fukuyama N., Yoshida K., Katayama Y. Ion solvation and water structure in an aqueous sodium chloride solution in the gigapascal pressure range. *J. Phys. Chem. Lett.* 2021. **12**(1): 250.
16. Otero L., Rodríguez A.C., Sanz P.D. Effect of the frequency of weak oscillating magnetic fields on supercooling and freezing kinetics of pure water and 0.9 % NaCl solutions. *J. Food Eng.* 2020. **273**: 109822.
17. Otero L., Rodríguez A.C., Sanz P.D. Effects of static magnetic fields on supercooling and freezing kinetics of pure water and 0.9 % NaCl solutions. *J. Food Eng.* 2018. **217**: 34.
18. Javadi S., Røyne A. Adhesive forces between two cleaved calcite surfaces in NaCl solutions: The importance of ionic strength and normal loading. *J. Colloid Interface Sci.* 2018. **532**: 605.
19. Wu Y., Wang Y., Hu L. A theoretical model of the soil freezing characteristic curve for saline soil. *J. Hydrology* 2023. **622**: 129639.
20. Tao Y., Yang P., Li L., Si X., Jin Y. Characterizing unfrozen water content of saline silty clay during freezing and thawing based on superposition of freezing point reduction. *Cold Regions Sci. Technol.* 2023. **213**: 103933.
21. Luan H., Wu J., Geng F., Zhao X., Li Z. Freezing characteristics of deicing salt solution and influence on concrete salt frost deterioration. *J. Adv. Concrete Technol.* 2023. **21**: 643.
22. Xiao Z., Lai Y., Zhang M. Study on the freezing temperature of saline soil. *Acta Geotechnica*. 2018. **13**: 195.
23. Ming F., Chen L., Li D., Du C. Investigation into freezing point depression in soil caused by NaCl solution. *Water*. 2020. **12**: 2232.
24. Zhao J., Gao X., Chen S., Lin H., Li Z., Lin X. Hydrophobic or superhydrophobic modification of cement-based materials: A systematic review. *Composites Part B*. 2022. **243**: 110104.
25. Koniorczyk M., Bednarska D. Kinetics of water freezing from inorganic salt solution confined in mesopores. *Thermochimica Acta*. 2019. **682**: 178434.
26. Sonoki Y., Pham Q.D., Sparr E. Beyond additivity: A mixture of glucose and NaCl can influence skin hydration more than the individual compounds. *J. Colloid Interface Sci.* 2022. **613**: 554.
27. Zhang X., Manica R., Tang Y., Liu Q., Xu Z. Bubbles with tunable mobility of surfaces in ethanol-NaCl aqueous solutions. *J. Colloid Interface Sci.* 2019. **556**: 345.
28. Sun K., Nguyen C.V., Nguyen N.N., Ma X., Nguyen A.V. Crucial roles of ion-specific effects in the flotation of water-soluble KCl and NaCl crystals with fatty acid salts. *J. Colloid Interface Sci.* 2023. **636**: 413.
29. Bozorgian A. An overview of methane gas hydrate formation. *J. Eng. Indu. Res.* 2021. **2**(3): 166.

30. Aregbe A.G. Gas hydrate properties, formation and benefits. *Open J. Yangtze Oil and Gas*. 2024. **9**(3): 27.
31. Ahmadi G., Smith D.H. Numerical solution for natural gas production from methane hydrate dissociation. *J. Petroleum Sci. & Engr.* 2004. **41**(4): 269.
32. Giavarini C., Maccioni F. Self-preservation at low pressures of methane hydrates with various gas contents. *Ind. Eng. Chem. Res.* 2004. **43**(20): 6616.
33. Sloan E.D. Jr. Fundamental principles and applications of natural gas hydrates. *Nature* 2003. **426**: 353.
34. Bouffaron P., Perrigault T. Methane hydrates, truths and perspectives. *Intern. J. Energy, Information and Communications*. 2013. **4**(4): 23.
35. Wu G., Ji H., Tian L., Chen D. Effects of salt ions on the methane hydrate formation and dissociation in the clay pore water and bulk water. *Energy & Fuels*. 2018. **32**(12): 12486.
36. Shen Y., Wei X., Wang Y., Shen Y., Li L., Huang Y., Ostrikov K.K., Q Sun C. Energy absorbancy and freezing-temperature tunability of NaCl solutions during ice formation. *J. Mol. Liquid*. 2021. **344**: 117928.
37. Lamas C.P., Vega C., Noya E.G. Freezing point depression of salt aqueous solutions using the Madrid-2019 model. *J. Chem. Phys.* 2022. **156**: 134503.
38. Li D., Zeng D., Yin X., Han H., Guo L., Yao Y. Phase diagrams and thermochemical modeling of salt lake brine systems. II. NaCl + H₂O, KCl + H₂O, MgCl₂ + H₂O and CaCl₂ + H₂O systems. *Calphad*. 2016. **53**: 78.
39. Yuan H., Sun K., Wang K., Zhang J., Zhang Z., Zhang L., Li S., Li Y. Ice crystal growth in the freezing desalination process of binary water-NaCl system. *Desalination*. 2020. **496**: 114737.
40. Fumoto K., Sato T., Kawanami T., Inamura T., Shiota M. Ice slurry generator using freezing-point depression by pressurization - Case of low-concentration NaCl aqueous solution. *Int. J. Refrigeration*. 2013. **36**: 795.
41. Gun'ko V.M., Turov V.V. *Nuclear Magnetic Resonance Studies of Interfacial Phenomena*. (Boca Raton: CRC Press, 2013).
42. Petrov O.V., Furó I. NMR cryoporometry: Principles, applications and potential. *Prog. Nuclear Magn. Reson. Spectr.* 2009. **54**: 97.
43. Mitchell J., Webber J.B.W., Strange J.H. Nuclear magnetic resonance cryoporometry. *Phys. Rep.* 2008. **461**: 1.
44. Kimmich R. *NMR Tomography, Diffusometry, Relaxometry*. (Heidelberg: Springer, 1997).
45. Gregg S.J., Sing K.S.W., Stoeckli H.F. (editors). *Characterization of Porous Solids*. (London: Soc. Chem. Industry, 1979).
46. Adamson A.W., Gast A.P. *Physical Chemistry of Surface*. Sixth edn. (New York: Wiley, 1997).
47. Gun'ko V.M. Textural characteristics of composite adsorbents analyzed with density functional theory and self-consistent regularization procedure. *Chemistry, Physics and Technology of Surface*. 2020. **11**: 163.
48. Cullity B.D., Stock S.R. *Elements of X-Ray Diffraction*. Third Edition. (New York: Prentice-Hall Inc., 2001).
49. Guinier A. *X-Ray Diffraction*. (San Francisco: WH Freeman, 1963).
50. de Avillez R.R., Abrantes F.G., Letichevsky S. On the intrinsic limits of the convolution method to obtain the crystallite size distribution from nanopowders diffraction. *Materials Research*. 2018. **21**(3): e20170980.
51. Popović S., Skoko Ž. X-ray diffraction broadening analysis. *Macedonian J. Chem. Chem. Eng.* 2015. **34**: 39.

52. Gun'ko V.M., Oranska O.I., Paientko V.V., Sulym I.Ya. Particulate morphology of nanostructured materials. *Chem. Phys. Technol. Surf.* 2020. **11**(3): 368.
53. Provencher S.W. A constrained regularization method for inverting data represented by linear algebraic or integral equations. *Comp. Phys. Comm.* 1982. **27**: 213.
54. Gun'ko V.M., Goncharuk E.V., Nechypor O.V., Pakhovchishin S.V., Turov V.V. Integral equation for calculation of distribution function of activation energy of shear viscosity. *J. Colloid Interface Sci.* 2006. **304**: 239.
55. Gun'ko V.M. Interfacial phenomena: effects of confined space and structure of adsorbents on the behavior of polar and nonpolar adsorbates at low temperatures. *Current Phys. Chem.* 2015. **5**(2): 137.
56. Mallamace F., Corsaro C., Broccio M., Branca C., González-Segredo N., Spooren J., Chen S.-H., Stanley H.E. NMR evidence of a sharp change in a measure of local order in deeply supercooled confined water. *Proc. Natl. Acad. Sci. USA.* 2008. **105**: 12725.
57. Gun'ko V.M., Turov V.V., Krupska T.V., Borysenko M.V. Surroundings effects on the interfacial and temperature behaviors of NaOH/water bound to hydrophilic and hydrophobic nanosilicas. *J. Colloid Interface Science.* 2023. **634**: 93.
58. Frisch M.J., Trucks G.W., Schlegel H.B., Scuseria G.E., Robb M.A., Cheeseman J.R., Scalmani G., Barone V., Petersson G.A., Nakatsuji H., Li X., Caricato M., Marenich A.V., Bloino J., Janesko B.G., Gomperts R., Mennucci B., Hratchian H.P., Ortiz J.V., Izmaylov A.F., Sonnenberg J.L., Williams-Young D., Ding F., Lipparini F., Egidi F., Goings J., Peng B., Petrone A., Henderson T., Ranasinghe D., Zakrzewski V.G., Gao J., Rega N., Zheng G., Liang W., Hada M., Ehara M., Toyota K., Fukuda R., Hasegawa J., Ishida M., Nakajima T., Honda Y., Kitao O., Nakai H., Vreven T., Throssell K., Montgomery J.A. Jr., Peralta J.E., Ogliaro F., Bearpark M.J., Heyd J.J., Brothers E.N., Kudin K.N., Staroverov V.N., Keith T.A., Kobayashi R., Normand J., Raghavachari K., Rendell A.P., Burant J.C., Iyengar S.S., Tomasi J., Cossi M., Millam J.M., Klene M., Adamo C., Cammi R., Ochterski J.W., Martin R.L., Morokuma K., Farkas O., Foresman J.B., Fox D.J. Gaussian 16, Revision C.02, Gaussian, Inc., Wallingford CT, 2019.
59. Barca G.M.J., Bertoni C., Carrington L., Datta D., De Silva N., Deustua J.E., Fedorov D.G., Gour J.R., Gunina A.O., Guidez E., Harville T., Irle S., Ivanic J., Kowalski K., Leang S.S., Li H., Li W., Lutz J.J., Magoulas I., Mato J., Mironov V., Nakata H., Pham B.Q., Piecuch P., Poole D., Pruitt S.R., Rendell A.P., Roskop L.B., Ruedenberg K. Recent developments in the general atomic and molecular electronic structure system. *J. Chem. Phys.* 2020. **152**: 154102.
60. Gordon M.S., Schmidt M.W. Advances in electronic structure theory: GAMESS a decade later, in *Theory and Applications of Computational Chemistry: the first forty years*, C.E. Dykstra, G. Frenking, K.S. Kim, G.E. Scuseria (Eds.) (Amsterdam: Elsevier, 2005, pp. 1167–1189).
61. Rürger R., Franchini M., Trnka T., Yakovlev A., van Lenthe E., Philippsen P., van Vuren T., Klumbers B., Soini N. *AMS 2024.102. SCM, Theoretical Chemistry*. (Amsterdam: Vrije Universiteit, <http://www.scm.com>).
62. Stewart J.J.P. *MOPAC 2022.1.1*. Stewart Computational Chemistry, web: [HTTP://OpenMOPAC.net](http://OpenMOPAC.net). Feb. 6, 2024.
63. Hourahine B., Aradi B., Blum V., Bonafé F., Buccheri A., Camacho C., Cevallos C., Deshayé M. Y., Dumitrică T., Dominguez A., Ehlert S., Elstner M., van der Heide T., Hermann J., Irle S., Kranz J. J., Köhler C., Kowalczyk T., Kubář T., Lee I. S., Lutsker V., Maurer R. J., Min S. K., Mitchell I., Negre C., Niehaus T. A., Niklasson A. M. N., Page A. J., Pecchia A., Penazzi G., Persson M. P., Řezáč J., Sánchez C. G., Sternberg M., Stöhr M., Stuckenberg F., Tkatchenko A., Yu V. W.-z., Frauenheim T. DFTB+, a

- software package for efficient approximate density functional theory based atomistic simulations. *J. Chem. Phys.* 2020. **152**: 124101.
64. Cui M., Reuter K., Margraf J.T. Obtaining robust density functional tight binding parameters for solids across the periodic table. *ChemRxiv*. 2024.
 65. Marenich A.V., Cramer C.J., Truhlar D.G. Universal solvation model based on solute electron density and on a continuum model of the solvent defined by the bulk dielectric constant and atomic surface tensions. *J. Phys. Chem. B* 2009. **113**: 6378.
 66. Pettersen E.F., Goddard T.D., Huang C.C., Meng E.C., Couch G.S., Croll T.I., Morris J.H., Ferrin T.E. UCSF ChimeraX: Structure visualization for researchers, educators, and developers. *Protein Sci.* 2021. **30**(1): 70.
 67. Avogadro 2. <https://two.avogadro.cc/>. Ver. 1.99. 2024.
 68. Zhurko G.A., Zhurko D.A. *Chemcraft* (version 1.8, build b726b). <http://www.chemcraftprog.com>.
 69. *Jmol: an open-source Java viewer for chemical structures in 3D* (Ver. 16.2.31). <http://www.jmol.org/>.
 70. Gun'ko V.M., Turov V.V., Pakhlov E.M., Krupska T.V., Charmas B. Effect of water content on the characteristics of hydro-compacted nanosilica. *Appl. Surf. Sci.* 2018. **459**: 171.
 71. V.M. Gun'ko, V.V. Turov, E.M. Pakhlov, T.V. Krupska, M.V. Borysenko, M.T. Kartel, B. Charmas, Water interactions with hydrophobic versus hydrophilic nanosilica. *Langmuir*. 2018. **34**(40): 12145
 72. Turov V.V., Gun'ko V.M., Pakhlov E.M., Krupska T.V., Tsapko M.D., Charmas B., Kartel M.T. Influence of hydrophobic nanosilica and hydrophobic medium on water bound in hydrophilic components of complex systems. *Colloid. Surf. A: Physicochem. Eng. Aspects*. 2018. **552**: 39.
 73. Gun'ko V.M., Turov V.V. Interfacial phenomena in nanostructured systems with various materials. *ChemPhysChem*. 2024. **25**(6): e202300622.
 74. Gun'ko V.M., Turov V.V. Colligative properties of various liquid blends vs. temperature under confined space effects in pores of different adsorbents. *Chemistry, Physics and Technology of Surface*. 2024. **15**(1): 3.

PACS 61.05.C-; 61.10.Eq; 61.43.Gt; 61.46.+w; 67.30.hp; 68.08.-p; 68.37.Og; 68.43.-h; 68.47.Gh
DOI: 10.15407/Surface.2024.16.085

ВЗАЄМОДІЯ КОНЦЕНТРОВАНИХ РОЗЧИНІВ НАСІЗ ГІДРОФІЛЬНИМ І ГІДРОФОБНИМ ПРОГЕННИМИ КРЕМНЕЗЕМАМИ

В.М. Гунько^{1,*}, М.В. Борисенко¹, А.П. Головань¹,
Т.В. Крупська^{1,2}, К. Вей², Дж. Женг², В. Янг², В.В. Туров^{1,2}

¹Інститут хімії поверхні ім. О.О. Чуйка Національної академії наук України,
вул. Олега Мудрака, 17, Київ, 03164, Україна, e-пошта: vlad_gunko@ukr.net

²Інститут мікро/нано матеріалів та приладів,
Технологічний університет Нінбо, 315211, КНР

У пористих середовищах ефект обмеженого простору (CSE) може впливати на температурну та міжфазну поведінку води та відповідних розчинів. Природа поверхні пористих або дисперсних твердих тіл може впливати на міжфазні явища, включаючи як CSE, так і криоскопічні ефекти, викликані колігативними властивостями розчинів. Сильні

зміни характеристик адсорбційних шарів зв'язаних рідин, особливо у вузьких порах або порожнечах між наночастинками, обумовлені зниженням активності розчинника. Тому представляє інтерес порівняння поведінки води та водних розчинів NaCl під впливом CSE гідрофільних та гідрофобних сорбентів. В цій роботі використано гідрофобний (AM1) та гідрофільний (A-300) пірогенні кремнезему (нанокремнезему) як представники високодисперсних сорбентів з різною природою поверхні, які характеризуються текстурною пористістю. Ця пористість спричинена порожнечами між непористими наночастинками (NPNP), що утворюють агрегати, агломерати агрегатів і видимі частинки (супра-NP структури) у порошках низької насипної щільності. Вихідні матеріали та відповідні оброблені системи із зв'язаною водою та NaCl/водою досліджували за допомогою методів: адсорбції азоту, мікроскопії, рентгенівської дифракції, інфрачервоної спектроскопії, термогравіметрії, реометрії, спектроскопії ядерного магнітного резонансу та квантової хімії. Воду, зв'язану з нанокремнеземом з NaCl або без нього, можна віднести до кількох типів: слабо (WBW, замерзає при $260\text{ K} < T < 273\text{ K}$) і сильно (SBW, замерзає при $T < 260\text{ K}$) зв'язана вода; слабо (WAW, хімічний зсув $\delta_H = 0.5\text{--}2\text{ м.ч.}$) і сильно (SAW, $\delta_H = 4\text{--}6\text{ м.ч.}$) зв'язана вода. WAW не спостерігається для систем A-300. Крім того, в системах вода/NaCl є замерзла (нерухома) вода, яка характеризується затримкою танення ($T > T_m$) при $273\text{ K} < T < 287\text{ K}$ (метастабільна вода, MSW). Появу MSW можна пояснити вивільненням (з деякою кінетичною затримкою) води, захопленої кристалітами NaCl, розчиненими при $T > T_m = 273.15\text{ K}$, при збільшенні кількості рідкої води з підвищенням температури. Різницю в CSE у пустотах у гідрофобних і гідрофільних супра-NP структурах для зв'язаної воді можна пояснити поверхневими функціональними групами $=\text{Si}(\text{CH}_3)_2$, які посилюють кластеризацію води, зв'язаної з AM-1. В цілому різниця в природі поверхні AM-1 і A-300 впливає на: (i) розподіл кристалітів NaCl за розмірами; (ii) температуру плавлення/кристалізації NaCl; (iii) залежність в'язкості та крутного моменту від швидкості зсуву (деформації); (iv) температура та міжфазна поведінка води та розчинів NaCl при $215\text{--}287\text{ K}$; та (v) вплив дисперсійних середовищ на зв'язану воду. Отримані результати представляють інтерес не тільки з теоретичної точки зору, а й з практичної, оскільки обидва кремнезему використовуються як компоненти композитів, що містять воду та NaCl (або інші солі) у різноманітних практичних застосуваннях у медицині, сільському господарстві тощо.

Ключові слова: гідрофобний пірогенний кремнезем, гідрофільний пірогенний кремнезем, концентровані розчини NaCl, вода на межах поділу, ефекти обмеженого простору, кріоскопічні ефекти, поведінка розчинів на межах поділу, температурна поведінка.